Scanning Tunneling Luminescence of Pentacene Nanocrystals

THÈSE N^{O} 4860 (2010)

PRÉSENTÉE LE 15 DÉCEMBRE 2010

À LA FACULTÉ SCIENCES DE BASE

LABORATOIRE DE SCIENCE À L'ÉCHELLE NANOMÉTRIQUE

PROGRAMME DOCTORAL EN PHYSIQUE

ÉCOLE POLYTECHNIQUE FÉDÉRALE DE LAUSANNE

POUR L'OBTENTION DU GRADE DE DOCTEUR ÈS SCIENCES

PAR

Alexander KABAKCHIEV

acceptée sur proposition du jury:

Prof. M. Q. Tran, président du jury
Prof. K. Kern, directeur de thèse
Prof. A. Fontcuberta i Morral, rapporteur
Prof. T. Greber, rapporteur
Prof. A. Schneider, rapporteur

ÉCOLE POLYTECHNIQUE
FÉDÉRALE DE LAUSANNE
Suisse
2010

to
Mariana and Alex,
for their love and support

Abstract

Organic semiconductors are promising materials for future electronic and electroluminescence applications. A detailed understanding of organic layers and nano-sized crystals down to single molecules can address fundamental questions of contacting organic semiconductors at the nanometer limit and obtaining luminescence from them. In this thesis, electroluminescence spectra from pentacene, a policyclic hydrocarbon (acene), are discussed. The luminescence is induced by the current from the tip of a scanning tunneling microscope (STM). Pentacene is an organic semiconductor which gained a lot of attention in technology because of its electronic properties suitable for applications in thin film devices. Moreover, recent fundamental studies employed pentacene as a standard to demonstrate sub-molecular resolution by scanning probe techniques. This work reports the first observation of light emission from nanometer-sized pentacene crystals grown on an ultrathin insulating layer on noble metal surfaces. Different STM-techniques are combined to characterize the individual systems studied with respect to topography, crystal structure, electronic properties and work function changes.

The initial step of the project was the implementation of an optical system for light collection from the tunnel-junction of a low-temperature STM. In the set-up, a novel approach based on the use of *in situ* adjustable lenses has been realized. Three lenses placed in the vicinity of the tip-apex allow light collection into three independent channels which can be used for versatile optical analysis.

An important part in the characterization of the organic system was to clarify the interaction between adsorbed molecules and substrates. We investigated individual pentacene molecules on different ultrathin insulator-metal systems. With the STM tip in tunnel contact, the molecules are situated in a double barrier junction formed by the insulating layer on one side and the vacuum gap on the other side. The metal surface and the STM-tip form the electrodes. The electronic properties of pentacene in this configuration have been characterized. Insulator-metal-systems, which provide a good electronic decoupling for pentacene from the metal, have been chosen as substrates for the growth of pentacene nanocrystals.

Using the sub-molecular resolution of the STM we resolved the structure of the top-layer of the pentacene nanocrystals and found that the crystal phase agrees with the pentacene bulk

structure. Moreover, the comparison of charge injection barriers between individual molecules and nanocrystals of pentacene indicates a significant change of electronic properties after the formation of ordered structure from the individual building blocks.

Optical spectroscopy of the emitted light reveals an excitonic emission from the nanocrystals, which is in very good agreement with photoemission spectra of macroscopic crystals. Although a highly localized current-injection by the STM tip is used for excitation, it can be concluded that the source of light emission is delocalized. In contrast to luminescence measurements reported for other organic materials in STM, the excitation is not localized on the individual molecule, into which a charge is injected by the STM-tip. Our study indicates the importance of inter-molecular coupling leading to a high mobility of the excited state which has to be considered in the framework of STM-induced luminescence.

A further result is the observation of the Stark shift of pentacene luminescence, that has so far not been measured at large electric fields of the order of 1V/nm. The evaluation of the Stark shift provides information on dipole and polarizability change during the decay of an exciton. The measured large dipole change of the lowest singlet exciton in pentacene indicates a mixing of the Frenkel exciton (FE) with a small contribution of charge-transfer (CT).

Finally, we developed a set-up for photon correlation measurements in the STM. The properties of photon statistics is a means which can unambiguously prove that the luminescence is due to a single-photon source, i.e. a light source which emits no more than one photon at a time. A typical example of such a source is the emission from a single molecule. We performed photon correlations measurements of the luminescence from pentacene and C_{60} nanocrystals. While the excitonic bulk emission of pentacene is not expected to represent a single photon emitter, we also did not observe anticorrelations in the case of C_{60} indicating the importance of the local environment in the STM-junction, e.g.the short distance to the metal electrodes.

Keywords: *STM-induced luminescence, pentacene nanocrystals, molecular electroluminescence, Stark effect, ultrathin insulating layer, scanning tunneling microscopy, ultra high vacuum*

Zusammenfassung

Organische Halbleiter sind Materialien, die sich als vielversprechend für Anwendungen in der Elektronik und in der Elektrolumineszenz erweisen. Ein detailliertes Verständnis von organischen Schichten und kleinen Nanometer-Kristallen bis zu einzelnen Molekülen kann fundamentale Fragen bezüglich Kontaktierung und Lumineszenzanregung von Nanostrukturen beantworten. In der vorliegenden Arbeit werden Elektrolumineszenzspektren von Pentazen, einem polycyclischen Kohlenwasserstoff aus der Gruppe der Azene, untersucht. Die Lumineszenz wird angeregt durch den Strom von der Spitze eines Rastertunnelmikroskops (engl. Scanning Tunneling Microscope, STM). Der organische Halbleiter Pentazen hat große Aufmerksamkeit im Technologiebereich auf sich gezogen, weil seine elektronischen Eigenschaften sich sehr gut für Anwendungen als Dünnschicht-Bauelementen eignen. Darüber hinaus wurde Pentacen in kürzlich veröffentlichten, fundamentalen Arbeiten als Standard eingesetzt, um submolekulare Auflösung in der Rastersondenmikroskopie zu demonstrieren. Diese Dissertation berichtet über die erste Beobachtung von Lichtemission aus Pentazenkristallen auf der Nanometerskala. Die Kristalle wurden auf ultradünnen Isolatorschichten auf Edelmetalloberflächen gewachsen. Verschiedene STM-Techniken wurden kombiniert um die einzelnen Systeme bezüglich Topographie, Kristallstruktur, elektronischer Eigenschaften und Austrittsarbeitsänderungen zu charakterisieren.

Die Anfangsphase des Projekts umfasste die Implementierung eines optischen Systems zum Sammeln des Lichts aus der Tunnelbarriere eines Tieftemperatur-STMs. In dem Aufbau wurde ein neuartiges Prinzip realisiert, bei dem *in situ* justierbare Linsen eingesetzt werden. Drei Linsen sind in der Nähe der STM-Spitze montiert, und ermöglichen die Lumineszenzsammlung in drei unabhängigen Kanälen, die für vielfältige optische Analysen verwendet werden können.

Ein wichtiger Schritt in der Charakterisierung des organischen Systems war die Aufkärung der Wechselwirkungen zwischen den adsorbierten Molekülen und der Substrate. Wir untersuchten einzelne Pentazenmoleküle auf verschiedenen Isolatorschicht-Metall Systemen. Mit der STM-Spitze in Tunnelkontakt, befinden sich die Moleküle in einer Doppelbarriere, die durch die dünne Isolatorschicht auf der einen Seite und das Vakuum auf der anderen Seite

ausgebildet wird. Die Metalloberfläche und die STM-Spitze dienen als Elektroden. Die elektronischen Eigenschaften von Pentazen wurden in dieser Konfiguration charakterisiert. Substratsysteme, die eine gute elektronische Abkopplung des Pentazen vom Metall aufweisen, wurden als Unterlage zum Wachstum von Pentazen Nanokristallen eingesetzt. Unter Verwendung der submolekularen Auflösung des STMs wurde die Struktur der obersten molekularen Schicht der Nanokristalle aufgelöst. Dadurch zeigte sich, dass die Kristallphase sehr gut mit der Volumenstruktur von Pentazen übereinstimmt. Der Vergleich der energetischen Barrieren für die Ladungsinjektion in einzelne Moleküle und Nanokristalle, zeigt eine signifikante Änderung der elektronischen Eigenschaften, sobald eine geordnete Struktur aus den einzelnen Bausteinen ausgebildet wird.

Optische Spektroskopie des emittierten Lichts zeigt exzitonische Lumineszenz der Nanokristalle, die sehr gut mit Photoemissionspektren makroskopischer Kristalle übereinstimmt. Obwohl die Ladungsinjektion, die zur Emissionsanregung genutzt wird, auf ein einzelnes Molekül an der Oberfläche beschränkt ist, kann man aus den Ergebnissen schließen, dass die Anregung nicht auf diesem einen Molekül lokalisiert bleibt. Unsere Studie deutet auf die wesentliche Bedeutung der inter-molekularen Kopplung, die zu einer hohen Mobilität des angeregten Zustandes führt, und auf dem Gebiet der STM-induzierten Lumineszenz berücksichtigt werden muss.

Ein weiteres Ergebnis der Arbeit ist die Beobachtung der Starkverschiebung der Lumineszenz von Pentazen, der zuvor nicht bei hohen elektrischen Feldern in der Größenordnung von 1 V/nm gemessen worden war. Die Auswertung der Stark-Verschiebung liefert uns Information über die Dipoländerung bei der Exzitonenrekombination. Die sehr groß ausfallende Dipoländerung des niedrigsten Singlet-Exzitons in Pentazen deutet auf eine Mischung von Frenkel Exziton (FE) mit einem kleinen Beitrag eines Ladungstransferexcitons (engl. charge transfer exciton, CT) hin.

Abschließend haben wir einen experimentellen Aufbau für Messungen von Photonenkorrelationen im STM realisiert. Die Photonenstatistik ist ein Mittel zum eindeutigen Nachweis von Einzelphotonenemittern, d.h. zur Überprüfung, ob eine Lichtquelle nicht mehr als ein Photon zur selben Zeit emittiert. Ein typisches Beispiel solch einer Lichtquelle ist ein emittierendes Molekül. Wir haben Photonenkorrelationsmessungen an Pentazen und C_{60} Nanokristallen durchgeführt. Während nicht zu erwarten ist, dass die exzitonische Volumen-Emission von Pentazen eine Einzelphotonenquelle darstellt, haben wir auch im Fall von C_{60} keine Antikorrelation beobachten können, was auf den Einfluss der

lokalen Umgebung in der STM-Tunnelbarriere, insbesondere der nahen Metallelektroden, hindeutet.

Schlüsselbegriffe: *STM-induzierte Lumineszenz, Pentazennanokristalle, molekulare Elektrolumineszenz, Stark Effekt, ultradünne Isolatorschichten, Rastertunnelmikroskopie, Ultrahochvakuum.*

Contents

Contents

1 Introduction

Organic semiconductors have made a strong entrance in nanoscale electronics and optoelectronics during the last decade. These materials emerged as promising candidates for use in energy-efficient solid-state luminescence devices [1,2,3]. Organic light emitting diodes (OLED's) made it possible to realize light sources even on flexible foils [4,5]. This opened up the way to a novel display technology. Recently, flexible plastic displays built of OLED-pixels have been demonstrated to show color videos while the display is being bent, curved or wrapped [6]. Such non-rigid devices cannot be realized by LCD- or plasma- technologies, which are still the standard for commercial monitors and TV screens today. In flexible optoelectronics, organic semiconductors are used on one hand as the light-generating (OLED) material, and on the other hand as organic thin-film transistors (OFETs) which electrically drive the display-pixels [7]. Although OLED devices do not show the same high performance as silicon or GaAs circuits, they can be easily produced by ink jet printing [8,9,10], a low cost technology, which may open up the way to mass production of electronic newspapers, wearable electronics and displays [11].

In a typical OLED architecture, the organic layer(s) are sandwiched between a transparent anode and a metal electrode [12,13]. From both electrode-sides, charges of opposite sign are injected into the organic layer. Then the charges form a bound electron-hole pair, called exciton, which can emit a photon when it decays. The relative position of molecular levels with respect to the electrode's Fermi levels determine the energy barriers for charge injection. A lot of effort has been made to tune the interface properties around the emitting organic layer in order to increase light emission efficiency [14,15]. Thus, exploring the intrinsic properties of organic molecules is an important step to improve device performance.

In order to face the technological challenges associated with new and smaller organic devices, a more profound understanding is needed. As a prime model system for investigating the properties of organic based devices, the hydrocarbon molecule pentacene has been the subject of numerous studies in science [16]. Thin films and crystals of pentacene have gained importance in organic electronics as OFETs due to their high charge carrier mobilities and the progress in growing solids with improved properties [17,18,7]. The extended conjugation and strong tendency to form well-ordered crystal polymorphs [19] are responsible for its success as a

semiconductor. Moreover, the functionality of an OFET based on pentacene can be extended by electroluminescence [20], realizing devices for highly integrated organic optoelectronic systems [21].

Beyond the investigation of device functionalities, a fundamental insight into the underlying physics at the interface between electrode and molecule is essential. A step from a macroscopic thin-film device down to the investigation of organic aggregates containing a much smaller number of molecules has to be made. This will help to better understand the device behaviour at dimensions on the scale of the individual molecules. On this nanometer scale, scanning probe techniques are the tools of choice due to their capability to resolve single organic molecules and their electronic orbitals. Impressive results using STM [22,23] and atomic force microscopy AFM [24] demonstrate sub-molecular imaging, revealing structural and electronic features of single pentacene molecules on a substrate. Unperturbed gas-phase-like electronic orbitals can, for example, be observed on a molecule adsorbed on an insulator [22]. These studies show that the position and the width of electronic levels are determined by their environment, which can be a metal, an insulator or an organic layer. Such microscopic understanding of energy level alignment at interfaces influenced by molecule-substrate interactions is of utmost importance for the efficiency of an OLED device.

In an STM set-up employed to study materials on the atomic scale, a tip with a curvature of several tens of nm and a tip apex consisting of a few atoms is used as a mobile electrode. The tip can be positioned precisely over an individual molecule on a surface and current-voltage spectra can be recorded [25]. A further great advantage of STM is the possibility to locally excite luminescence [26]. Inelastic processes induced by the tunnel current of the STM-tip lead to light emission from tip-induced surface plasmons of the metal as well as intrinsic molecular fluoresecence [27,28,29]. Optical spectra obtained by charge injection into molecules show features that are due to electronic transitions of the particular molecule. So far, the number of chemical substances studied by STM-induced luminescence is still small. However, the method will be suitable for chemical recognition at the nanoscale due to the obtained molecule-specific optical spectra [28]. By the strong localization of the tunnel current from the STM-tip, charge injection is confined to individual molecules, which can result in sub-molecular spatial resolution of light spectra [27,30].

The injection of charges by STM into thin organic films realizes an electroluminescence device in which the current flows perpendicular to the film plane, a configuration similar to the one of an OLED. An important prerequisite for downscaling to nanometer dimensions is the electronic decoupling from the metal electrodes. The strong interaction between molecules

and metal can lead to quenching of fluorescence [31]. Thus, buffer layers of ultrathin insulators, as well as multilayer organic structures have been employed to make the fluorescence observable [29,28,32]. The goal of this work is to combine the capabilities of the STM technique to characterize the molecular system with respect to topography, electronic properties, local environment and electroluminescence characteristics. We extend experiments by STM-induced luminescence to a new class of chemicals, the acenes, taking pentacene as an example [19]. An important goal is to study the role of decoupling by different insulators on the molecule's electronic levels. We investigate the conditions of light emission, in particular its dependence on excitation voltage, current, and organic structure size.

The organization of the thesis is as follows. Chapter 2 is dedicated to the experimental technique employed in the thesis. In the first part, the principles of scanning tunneling microscopy and spectroscopy are briefly introduced. The features of the low-temperature STM, as well as different sample and tip preparation methods are presented at the beginning of Chapter 3. The main part of Chapter 3 introduces the optical system, which was assembled and implemented in the STM during the time of this thesis. A detailed description of the working principle for light collection from the STM-tunnel junction is made together with examples of various methods of luminescence characterisation.

In chapter 4 we discuss the use of ultrathin insulating layers of KCl and of the BN-nanomesh in order to obtain electronic decoupling of pentacene from the metal substrates of Au(111), Cu(111), Rh(111) and Cu(110). A comparison between KCl on close-packed and open metal surfaces is made. We demonstrate that not only the chemical composition of the insulator material is important, the buffer layer structure itself can play a decisive role determining its electrical properties.

At the beginning of Chapter 5, we introduce the growth and structure of pentacene nano-scale crystals on ultrathin KCl. The main part of the chapter is dedicated to optical spectroscopy of the STM-induced luminescence on the nanocrystals. A bulk-like excitonic spectrum typical for macroscopic crystals is observed, which strongly differs compared to single molecule emission lines reported so far. This contrasts with an assumed single molecular emission from the molecule into which the charge is directly injected by the STM tip. The study is extended in Chapter 6 by the evaluation of the Stark shift of the main luminescence peak. The shift is remarkably large, which, on the one hand, is due to the strong electric field inside the pentacene layer, but, on the other hand, indicates an unexpectedly large dipole moment of the exciton.

1 Introduction

Photon correlation measurements of STM-induced luminescence are presented in Chapter 7. After a short introduction to Hanburry-Brown and Twiss interferrometry and photon statistics, the experimental set-up for photon correlation analysis in the STM is introduced. Correlation measurements are shown for pentacene and C_{60}. For pentacene, an anticorrelation feature is not observed, as expected, due to the assignment of the emission line to a bulk exciton. The absence of the feature also for the C_{60} layer, which is assumed to exhibit emission from single molecules requires a detailed discussion.

Finally, the outlook suggests future experiments by STM-induced luminescence. In particular, conditions for the realization and observation of a single photon source below the STM tip will be discussed.

2 Principles of STM and STM-induced light emission

2.1 Scanning Tunneling Microscopy (STM).

The scanning tunneling microscope is a widespread surface science tool capable of achieving atomic resolution on a clean conductive substrate. A sharp metallic tip is brought to a distance of 5 Å – 20 Å from the substrate and a bias voltage is applied between them. As a result, a DC current flows through the vacuum gap between the two electrodes. This process, called tunneling, is described by quantum mechanics, taking into account the wave-like properties of the electrons. If an electron with energy E and mass m_e moves towards a barrier of constant height U, its wave function inside the barrier has the form [33]:

$$\psi(z) = \psi(0)e^{-\kappa z}, \tag{2.1}$$

with the decay constant κ

$$\kappa = \frac{\sqrt{2m_e(U-E)}}{\hbar}, \tag{2.2}$$

The electron wave function at the surface of one of the metal electrodes decays exponentially into the vacuum region (s. Fig. 2.1 left). When the metal tip is close to the sample, thus z is sufficiently small, there is a finite probability P to find the electron behind the vacuum barrier of thickness z.

$$P \propto |\psi(0)|^2 e^{-2\kappa z}, \tag{2.3}$$

For a small bias voltage, the effective potential barrier felt by the electron can be roughly approximated to be equal to the average work function of surface and tip $\Phi = (\Phi s + \Phi t)/2$, i.e. $U - E \approx \Phi$. This approximation implies that the vacuum barrier is described as a square barrier. In reality, there is, first, a small tilt of the vacuum potential due to the applied voltage, and, second, image forces acting on the electrons, which round off the potential edges. At voltages about 100 mV, the potential tilt can be neglected, since it is small compared to the barrier height, which is typically several eV [34]. However, the rounding of the barrier potential has to be taken into account for a more accurate modelling of the apparent barrier height in

STM [35]. It turns out that the image potential contribution lowers the effective potential height compared to the mean work function for tip-sample separations commonly obtained experimentally.

When a bias voltage is applied, the Fermi levels of tip and sample are shifted with respect to each other. As a result, a net tunneling current between tip and sample takes place. If, for example, a negative voltage with respect to the sample is applied, the tunneling current in the STM results as a product of the filled states of the sample and the empty states of the tip. However, the tip states are unknown, since the configuration of the tip apex consisting of a small number of atoms is not defined. In order to evaluate the tunneling current, a simple model was developed by Tersoff and Hamann [36]. They approximated the tip geometry as a sphere and used an s-like wave function to describe its electronic configuration. Thereafter the current I is proportional to the energy integral over the product of the local density of states (LDOS) of tip and sample ρ_t and ρ_s, the Fermi distributions f, and the transmission probability T.

$$I(V,z) \propto \int_0^{eV} \rho_s(E)\rho_t(eV-E)T(E,eV,z)\left[f(E-eV,T) - f(E,T)\right]dE\,, \tag{2.4}$$

The Fermi functions *f(E-eV,T)* and *f(E,T)* describe the Fermi distributions of the tip shifted by the bias to energy eV and the sample at the Fermi energy. The transition tunneling probability T reads as

$$T(E,V,z) = e^{\left(-2z\sqrt{(m_e/\hbar^2)\cdot(\Phi_s+\Phi_t-2E+eV)}\right)}, \tag{2.5}$$

with Φ_S and Φ_T the sample and tip work functions, respectively. If the bias voltage is small compared to the work function, eq. (2.4) can be simplified. The energy and bias dependence of T can be neglected. Furthermore, at low temperatures the Fermi-Dirac distribution can be approximated as a sharp step. Finally, the current takes the form:

$$I(V,z) \propto e^{\left(-2z\sqrt{(m_e/\hbar^2)\cdot(\Phi_s+\Phi_t)}\right)} \int_0^{eV} \rho_s(E)\rho_t(eV-E)dE\,. \tag{2.6}$$

Equation 2.6 reveals two contributions to the tunneling current and thus to the imaging process of the STM. The pre-exponential factor takes the exponential current dependence of the distance z into account. A second contribution comes from the integral, which describes the influence of the sample- and tip-LDOS.

The experimental realization of an STM is shown in Fig 2.1 on the right. The tip is mounted on a piezo crystal comprising 4 independent parts. The 2-dimensional scanning motion in the

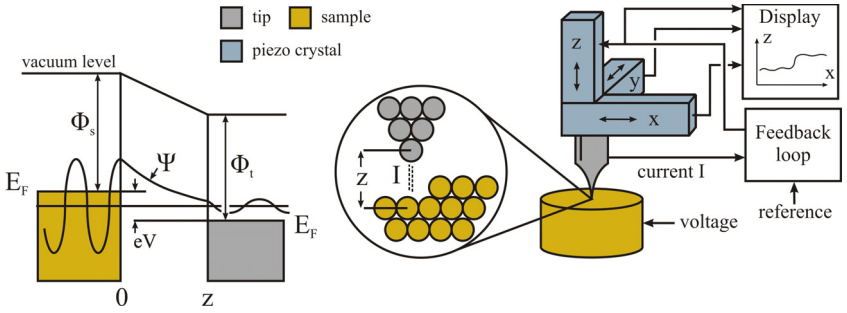

Figure 2.1. Principle of STM. Left: Wavefunction of an electron tunneling from sample to tip upon bias application. Middle: Enlarged view of the tunneling junction. The configuration of the tip-apex is generally unknown. Right: Schematic configuration of the experimental realization of an STM [37]. The scheme is based on [34, 33].

directions *x,y* is done by applying an alternating high voltage to the corresponding piezo segments.

An additional piezo crystal controls the displacement of the tip in the direction *z* towards the sample. In the constant current mode the tunneling current is kept constant by an electronic feedback loop, which regulates the tip-sample distance *z*. The STM-topography image is a plot of the resulting displacement *z* necessary to maintain a constant tunnel current at each scan point *(x,y)* of the lateral position. In the constant-height mode of operation, the feedback loop is switched off and the tip scans the sample at a predefined tip-sample distance *z*. In this case the 2-dimensional plot of the resulting current-signal is used for imaging.

2.2 Scanning Tunneling Spectroscopy (STS).

According to eq. (2.6), there are contributions to the tunneling current from the energy range below *eV* set by the applied bias voltage *V*. In order to gain information on the local density of states at a particular energy, spectroscopy is normally performed using the lock-in technique as a function of bias. The tip is fixed at a position of interest on the surface and under open feedback-loop the current is recorded. In our case the bias voltage is modulated by 20 meV amplitude and 750 Hz frequency and the differential conductance *dI/dV* is recorded simultaneously by a lock-in amplifier. The *dI/dV* signal can be approximated by

$$\frac{dI}{dV} \propto \rho_s(eV)\rho_t(0)\,. \qquad (2.7)$$

Equation 2.7 implies that the transmission coefficient T and ρ_t are independent of V if V is small. Then the dI/dV signal is proportional to the LDOS at the particular tip position. However, in order to obtain the pure LDOS of the sample, the density of states of the tip has to be flat, i.e. without sharp features.

STS is used to study the electronic properties of adsorbates deposited on an ultrathin insulator/metal surface like organic molecules [22]. In this case, the molecule's frontier orbitals, namely, the highest occupied (HOMO) and the lowest unoccupied (LUMO) molecular orbitals, can be accessed. These orbitals represent localized states, which can be energetically far away from the metal's Fermi-level. During a spectroscopic voltage sweep, a resonant tunnel condition can be passed, which means that the energetic position of the particular molecular level is equal to the electron energy set by the bias. This gives rise to peaks in the dI/dV signal, as a function of bias. The peak position gives information about the molecular level alignment on the particular substrate. An interesting effect observed in the spectroscopic measurement is a negative differential conductance at energies beyond the resonant tunneling condition into the molecular level [38,39,22]. It arises due to the increase of the tunneling barrier for tunneling into the molecular orbital when the voltage increases and is not an intrinsic feature of the molecule-substrate system [22].

Another type of spectroscopic technique in the STM is used to determine the local barrier height [34]. This is done by fixing the tip-sample distance at a set-point of small voltages and currents and subsequently opening of the feedback loop. Then the tip-sample distance z is linearly reduced and the current is recorded. Following (2.5) the transition coefficient can be defined as the ratio of the current at the tip surface at a vacuum barrier of z and at the sample surface for $z = 0$

$$T = \frac{I(z)}{I(0)} e^{-2\kappa z}, \tag{2.8}$$

If a small bias is used according to (2.2) and (2.8), the average work function $\Phi = (\Phi s + \Phi t)/2$ can be expressed as

$$\Phi = \frac{\hbar^2}{8m_e}\left(\frac{d \ln I}{dz}\right)^2. \tag{2.9}$$

The average work function is thus obtained from the slope of the logarithm of the current as a function of the tip-sample distance. A typical value of the work function of 5 eV (e.g. Au tip on Au(111) surface) gives a decay constant $\kappa = 11.4\ nm^{-1}$ [34]. According to (2.9), the tunnel current decays by one order of magnitude if z increases by 0.1 nm.

2.3 STM-induced light emission

The first experimental observation of light emission from a tunneling junction dates back to 1976, the work of Lambe et al. [40]. A metal-oxide-metal (MOM) sandwiched structure was used for this first experiment. Upon biasing the junction with voltages of a few volts, light emission in the visible range with a broad spectral shape took place. In the proposed model, an electron tunneling inelastically through the thin insulator from one metal to the other excites a radiative plasmon mode in the junction with frequency υ. A characteristic feature of emission spectra is the quantum cut-off, provided that $|eV| \geq h\upsilon$, where eV is the electron energy defined by the applied voltage V.

Shortly after the invention of the STM, light emission from its tunnel junction was demonstrated [26]. These results were achieved on polycristalline tantalum and Si(111)7x7, and their emission line at 9.5 eV has been shown to obtain similar information as inverse photoemission spectroscopy, however, with the high spatial resolution typical for STM. In the following years, experimental and theoretical works on STM-induced luminescence from metal tips and noble metal substrates led to a profound understanding of the excitation process [41,42,43]. It was established that the emission is due to the radiative decay of tip-induced surface plasmons (TIP) excited by inelastic electron tunneling (IET) (Fig. 2.2 a) [41]. These plasmons are collective electron oscillations, in which the free electrons of tip and surface are coupled by electromagnetic interaction in the nanocavity of the STM-tunnel junction. The emission yield was proposed to be in the order of 10^{-3}-10^{-4} photons per tunneling electron [44]. Typically, plasmonic spectra are very broad. Apart from their characteristic energy cut-off, the emission yield and energy distribution further depend on the tip-sample distance, tip and sample material and tip geometry. The strong localization and spatial resolution achieved by STM-induced light emission makes the technique a sensitive probe for electromagnetic interactions on the nano-scale [45]. Intrinsic plasmon resonances from metal nanoclusters of Ag and Au decoupled by an ultrathin insulating layer in the STM-junction have been observed [46,47]. The investigation of inelastic tunneling processes became possible even on the atomic scale, visualized by photon-maps, taken simultaneously during the scan. Standing wave patterns in the photon-maps induced by confined electron states on metal surfaces were reported for Au nanostructures on Au(111) [48] and Ag atomic chains on NiAl(110) [49].

STM-induced luminescence has proven suitable to study also radiative electronic transitions in semiconductor materials [50,26]. The spatial dependence of the electroluminescence excitation process was reported recently for GaAs even with a resolution down to the atomic scale [51].

The first study to use STM for luminescence excitation from molecules has been carried out on C_{60} deposited directly on Au(111) [52]. The authors observed a structure in the photon-map taken during a constant-current-scan over a molecular monolayer. The regions of maximal intensity correlate with the position of the molecules, which strongly suggests that the molecules are involved in the emission process. Later on, first optical spectra of STM-induced luminescence were reported for conjugated polymer films of poly(*p*-phenylenevinylene) deposited on glass [53]. However, normally when molecules are adsorbed directly on a bare metal surface, the fluorescence is strongly reduced due to non-radiative energy dissipation, as shown by earlier experiments [31]. Thus, the molecules have to be decoupled from the metal substrate in order to minimize quenching effects. Following this approach, vibrationally resolved luminescence from ZnEtiol molecules adsorbed on a thin oxide layer on NiAl(110) surface has been achieved in the STM [27]. The emission was attributed to transitions between unoccupied orbitals of the molecule, which was negatively charged. Intrinsic luminescence associated with HOMO-LUMO transitions of C_{60} was demonstrated by optical spectroscopy on C_{60} nanocrystals [28]. The nanocrystals were deposited on an ultrathin insulating layer of NaCl on Au(111). Another successful approach for decoupling is the usage of multilayers of the same molecule as decoupling phase for the molecules in the top-layer. In such a configuration intrinsic luminescence from porphyrins has been demonstrated for thin films of 6 monolayers height [29,54].

Concerning the mechanism of molecular electroluminescence excitation in the STM-junction, there are three relevant processes discussed in the literature by now. Resonant tunneling into the molecular orbitals from both electrodes (s. Fig 2.2. b) leads to a simultaneous injection of a charge into a higher orbital and a charge extraction from a lower-lying orbital [28,27]. As a consequence, an electron-hole pair is formed, which can undergo a radiative recombination. A second channel of fluorescence generation is inelastic tunneling into the metal substrate, which excites surface plasmons. Since both processes can take place, optical spectra have to be carefully analyzed in order to distinguish the intrinsic molecular luminescence from the eventually present plasmonic background. Plasmon modes have been further shown to enhance molecular fluorescence [32]. However, this leads to a modification of the fluorescence spectra depending on the intensity profile of the plasmon resonance and the spectral overlap between both. Recently, a new type of excitation process, called upconversion luminescence, has been reported for porphyrin films [54]. It leads to a light emission of higher energy compared to the excitation energy defined by the bias voltage.

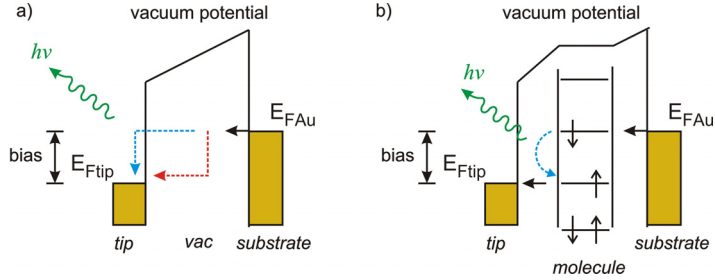

Figure 2.2. Mechanism of light emission in the STM junction. Inelastic electron tunneling (a) gives rise to Plasmon excitation and emission. Blue and red arrows indicate two possible paths of electron energy-loss, blue: in the vacuum region, red: in the metal (also called hot-electron tunneling). (b) Resonant tunneling into molecular orbitals placed within the tip-sample junction initiates an electronic transition and fluorescence excitation [27,28,30].

In the above-mentioned works, the emission spectra could be identified and there was a good agreement with measured photoluminescence spectra of the same molecules. These studies have shown the ability of STM-induced light emission to obtain chemical identification on a single molecule scale.

However, there are several issues which have not been addressed in these works. The reported results on molecular structures of nanocrystals and thin films suggest that individual molecules in the top-layer addressed by the tip are the source of light emission [28,54]. This means that the excitation is localized on a particular molecule and no energy transfer to neighbouring molecules takes place. Such an effect is likely to happen if the molecular coupling within the aggregate is very weak. An unambiguous proof whether the excitation is localized is the observation of anticorrelation in the photon statistics of the emitted light [55]. This effect is discussed in detail in Chapter 7 of the thesis. Photon anticorrelation, so far not reported for STM-induced luminescence, would demonstrate the presence of a single-molecule as light-source. In the present work it will be shown that an intermolecular coupling of high strength can lead to an emission not localized on one particular molecule. Pentacene is known for the strong intra-molecular interaction within an ordered phase. In nanocrystals it shows luminescence due to excitons typical for macroscopic crystals, which can radiate from different sites inside the crystal volume. Thus, the charge-injection site does not coincide with the radiation site.

Furthermore, the influence of the electric field naturally present within the STM-gap has not been exploited to obtain information on molecular transitions so far. The energy dependence

of the emission upon field variation (Stark effect) gives important information on the dipole strength of the excited state. This issue will be addressed in the present work and discussed in detail in Chapter 6.

3 Experimental set-up

The study of organic molecules presented here involves high resolution imaging in the STM as well as electronic spectroscopy. For a good signal-to-noise ratio, optical spectroscopy is performed for an extended period of time (up to hours) at a fixed point of the STM-tip. In order to be able to do this, high stability during operation of the microscope is necessary. Furthermore, diffusion of the molecules on the substrate has to be strongly reduced. Such conditions can be realized by measurements at low temperatures down to 4 K, which provides thermal stability of the set-up as well as low mobility of the molecules.
As part of the thesis, an optical system was built and implemented into an existing low-temperature STM. First, the features of the STM and the sample preparation will be shortly described. In the second part of the chapter, the optical system set-up will be discussed in detail, followed by examples of different modes of measurements on luminescence from the STM junction.

3.1 The STM set-up

3.1.1 Low-temperature STM

The experiments in the thesis were performed in a home-built STM (Fig. 3.1), operating at liquid He temperatures constructed during an earlier PhD thesis [56]. The entire set-up comprises two ultra high vacuum (UHV) chambers. The UHV pressure is maintained by turbomolecular pumps (Leybold Vacuum, Pfeiffer), as well as ion pumps (Varian). The chamber used for sample preparation is separated from the STM-chamber by a gate-valve. The STM-chamber has a base pressure lower than 1.10^{-11} mbar.
Mechanical stability is provided by two passive damping stages (Newport) and an active damping stage (Stacis 2100, TMC, Peabody, USA) (s. Fig. 3.1 a). The system-frame, on which the UHV-chambers are mounted, is mechanically decoupled by the lower passive dampers from the actively damped massive base-plate. For an additional vibrational isolation, the cryostat holding the STM is attached to a platform, which is additionally decoupled from

the STM-chamber by the upper passive dampers. The resulting vibrational noise of the tip-sample junction during operation is in the order of 2 pm.

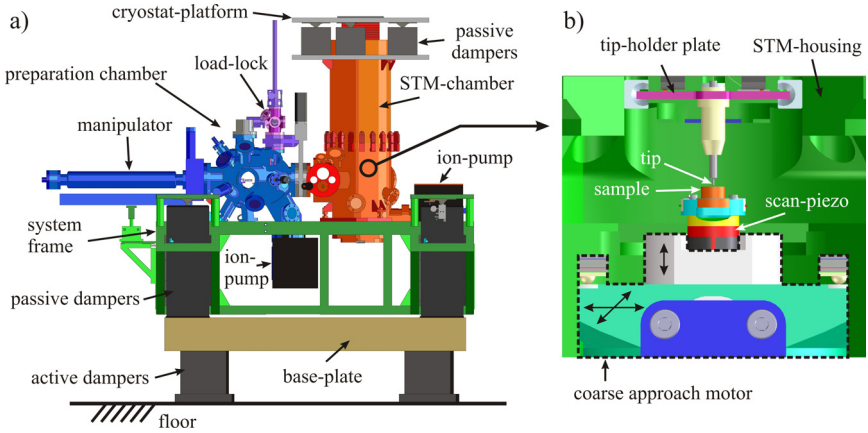

Figure 3.1. (a) Illustration of the set-up. The two UHV-chambers (blue: Preparation chamber; orange: STM chamber) separated by a valve are mounted on a steel frame (green). The cryostat is mounted on a thick steel plate. The preparation chamber has a load-lock for transferring samples and tips from the outside, which are transferred to the STM chamber by the manipulator. (b) Inner view of the STM-head (green).

The bath cryostat of the instrument has a volume of approx. 8 liters enabling continuous measurements for 3 days. Heat-flow from the environment is reduced by radiation shields cooled by liquid nitrogen.

The STM configuration is depicted in Fig. 3.1 b. It comprises an exchangeable plate, which holds the tip (top) and an exchangeable sample mounted in a magnetizable sample holder (bottom). The sample holder is held in position by a magnet glued to a 8 segment scan piezo (supplier: Stavely sensors Inc., USA). One ring of 4 segments is employed for horizontal scanning, and 4 segments are interconnected to control the tip-sample distance (vertical offset during scanning). The scanning unit is mounted on a home-built coarse approach motor [56], which allows horizontal and vertical positioning over a range of several millimeters.

3.1.2 Sample and tip preparation

In the present study noble metal single crystals were employed as substrates in the STM. Their surfaces have a defined lattice face, obtained by an appropriate cut of the crystal (MaTek GmbH, orientational misfit < 0.1°). Close-packed low index surfaces of Au(111), Cu(111), Ag(111), Rh(111) as well as Cu(110) were used as templates. In order to achieve high resolution in STM, atomically flat, well-defined substrate-surfaces are necessary. Therefore, the metal surfaces have to be cleaned *in situ*, under UHV conditions prior to the deposition of the adsorbates. This is done in a dedicated preparation chamber attached to the STM-chamber. The metal substrates are cleaned by Ar^+-sputtering cycles followed by annealing. Typical parameters are an Ar^+-ion energy of 900 V, sputtering time of 20 min and an ion current of 19 µA detected on the sample. In order to avoid impurity diffusion from the crystal volume towards the surface, the annealing temperature is gradually reduced by 10 K or 20 K from 850 K to 800 K (for Au, Cu and Ag crystals) and from 1130 K to 1100 K (for Rh) with each cleaning cycle.

Organic molecules were deposited onto an ultrathin insulating layer of KCl or BN-nanomesh for electronic decoupling from the metal. Except for the BN layer, all the components are prepared by thermal evaporation. The preparation chamber is equipped with home-built evaporators, where the effusion cells containing the molecules and the KCl are heated by electron bombardment. The KCl is deposited onto the freshly cleaned metal surface kept at room temperature. In this way, an ultrathin layer comprising 1-3 monolayers of crystalline KCl on the metal surface can be prepared [56].

The boron nitride layer is prepared by a high-temperature exposure of the Rh(111) surface to borazine $(HBNH)_3$ as described in reference [57]. First, the freshly cleaned Rh(111) is heated up and kept at a temperature of 1100 K. Then borazine is let into the preparation chamber at a pressure of 3.10^{-7} mbar for 30 s. Afterwards the sample is cooled down and transferred to the STM for analysis. This preparation procedure leads to a complete coverage of the Rh(111) surface by one monolayer of BN.

Essential for the measurements in the STM is a good metallic tip, free of impurities at the tip-apex. This is usually achieved by tip-preparation on a clean metal substrate. However, the studied molecular samples comprise an extended layer of an insulator and a high coverage of molecules, thus there are no free metal regions usually left. In order to have the opportunity to reproducibly prepare and recover the tip on a clean metal, we employed a shutter covering half of the crystal surface during KCl- and molecule-deposition. In this way 50% of the metal

substrate was left clean and free from adsorbates. Then the tip could be repeatedly prepared for STM and light emission measurements on the clean metal side by moving the tip only by a few mm on the same sample. The coarse approach motor moves the sample laterally over about 3 mm, which allows quick *in situ* switching between the clean metal and the molecule/insulator system of interest. As tips we used electrochemically etched W- and Au-tips [58]. The W-tips were additionally *in situ* coated with silver in the preparation chamber. A melting-pot containing silver was heated up to 1150 K, and the W-tip was held directly above the hot silver-surface for 10 min.

3.2 Introducing a versatile optical access to the STM-tunnel gap

We developed a set-up providing three independent optical access paths to the tunnel junction of the low-temperature STM. Each path can be individually chosen to couple light in or out, or to image the tip-sample region. The design comprises *in situ* adjustable aspheric lenses to allow tip exchange. The heat input due to thermal radiation into the STM is negligible. We present in detail the beam geometry and the realization of lens adjustment. Measurements demonstrate the characterization of a typical light source exemplified by emission from tip-induced plasmons. We suggest employing the Fourier transforming properties of imaging lenses and polarization analysis to obtain additional information on the light emission process. Performance and future potential of the instrument are discussed.

3.2.1 Introduction

The observation of luminescence stimulated by the localized tunnel current in a scanning tunneling microscope has become a valuable technique for the characterization of tip-induced plasmon emission from metal surfaces [26,41], semiconductor quantum structures [50], and molecules adsorbed on surfaces [27-29]. The combination of light spectroscopy with electronic tunneling spectroscopy can provide deep insight into excitation mechanisms of adsorbed molecules [30]. The experimental technique allows the combination of the high spatial localization of the injected tunnel current (< 1nm) with the virtues of optical spectroscopy. The latter provides a performance which is not achieved by STM alone: (1) high relative energy resolution ($\lambda/\Delta\lambda > 10^3$) using optical spectrometers, (2) characterization of the light emitting process by light polarization analysis [59] and (3) luminescence time correlation measurements [60].

3 Experimental set-up

Instrumental designs which serve the previously discussed or similar types of experiments have been presented by different groups [47, 61-65]. Our approach to optimize light detection continues these developments and adds several new perspectives. Polarization analysis and time correlations of the emitted light can be fully exploited only if free propagating light beams are used instead of beams guided by optical fibres. In addition, free propagating beams preserve the angular emission distribution of the light source, which we will discuss in detail below. Low temperature set-ups have been realized earlier, e.g., by separate cooling of an externally adjusted lens to liquid nitrogen temperature [61,66], collecting by optical fibres [67], or the use of a conductive transparent tip attached to a fibre [68]. Maintaining the instrument constantly at liquid He temperature while using free propagating beams requires a new design, which restricts thermal input into the STM.

The goal of maximized light collection efficiency can be achieved by employing an ellipsoidal [69] or parabolic mirror [47] surrounding the tip-sample region. Such a solution also allows completely eliminating chromatic aberration. Our aim to integrate a highly versatile optical set-up into an already operating STM system with the important features of tip and sample exchange, easy optical adjustment, and high mechanical stability leads us to a compromise providing still fairly good collection efficiency and achromaticity.

3.2.2 Basic design idea

The set-up presented in this thesis requires a full (3 translational degrees of freedom) *in situ* re-adjustment of the collecting optics with respect to the STM-tip over a range of at least 0.3 mm (positional variation of different tips) and a precision of adjustment of about 10 μm (a few times the optical resolution). The optics is cooled to the same temperature as the whole STM assembly and heat input is very efficiently suppressed by focusing the light from the tunnel junction through two small holes which serve to confine also the solid angle for radiation input from the room temperature environment.

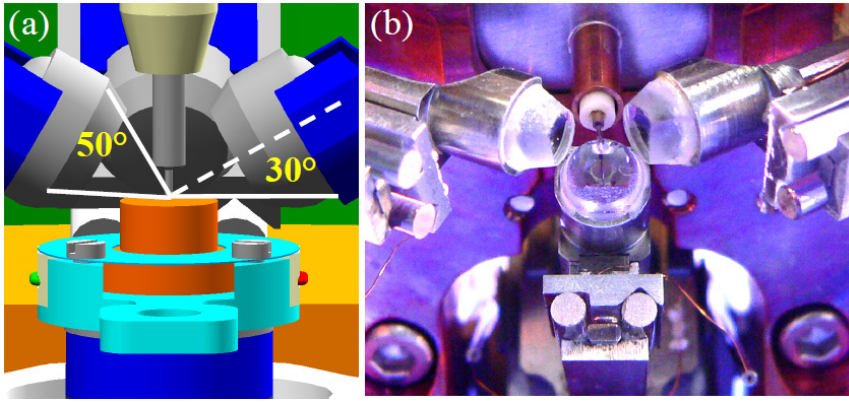

Figure 3.2. (a) Computer aided design (CAD) image [70] of the lens arrangement near the tip-sample tunnel junction. The optical axes form an angle of 30° with respect to the surface plane. The acceptance angle of each lens is 50°. (b) Photograph of the assembly of the tip and the three lenses without a sample.

We chose a geometry (Fig. 3.2 a, b) with three aspheric lenses mounted at azimuths 90° from one another and their optical axis at 30° elevation angle from the sample plane. Each lens has a numerical aperture (N.A.) of 0.42 yielding a collecting area of 9,2% of the half sphere per lens. The total solid angle of light collected from the tunneling gap is, however, not the most relevant figure because, first, luminescence emission towards the surface normal is not possible due to blocking by the STM tip itself and second, the emission intensity at grazing angle tends towards zero. More relevant is, in fact, the collection of light around the elevation of maximum emission which is situated approximately 60° off the surface normal [61]. From the light emitted on the 60° cone the three lenses collect 47 % of the light. A higher value would be achieved if the lens axes were separated by angles smaller than 90°. However, for a better interpretation of measurements we decided to provide clearly defined parallel (180°) or orthogonal (90°) observation directions when projected onto the sample surface. Reflection losses at the uncoated surfaces of lenses and viewports can in total add up to 20%-25%. We thus estimate a total collection efficiency of 21% and 35% for the two limiting cases of isotropic radiation and radiation exclusively on the 30° cone, respectively. As will be discussed in section 3.3.5, the chromatic aberration can lead to additional wavelength-dependent losses for wavelengths for which the focus is not optimized.

We remark that the exchange of tip and sample requires full access from one side so that one quarter of the cone cannot be equipped with a light collection unit. The commercial lenses

(for details, see section 3.2.5) were polished on their sides to obtain a conical shape near the entrance face (see Fig. 3.2 b) which avoids mechanical collision between adjacent lenses and collision between lenses and sample surface. In fact, the optical performance is not remarkably impaired by this treatment and the numerical aperture is not reduced.

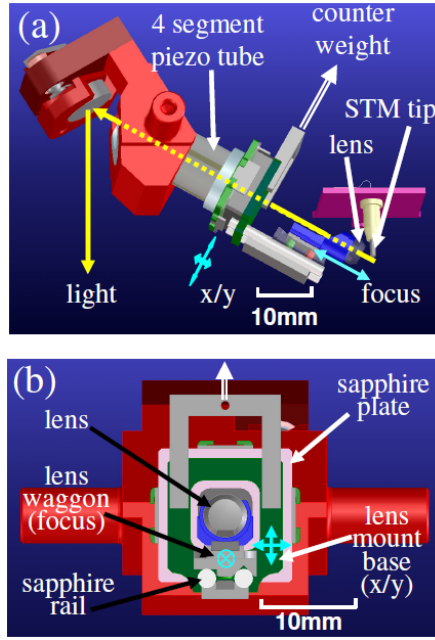

Figure 3.3. CAD images [70] of one of the three lens adjustment units. The individual parts of the assembly are separately colored. (a) Side view with tip holder, (b) head-on view in the direction of light propagation. The principal parts are described in the text.

Fig. 3.3 shows in detail the unit carrying one lens. Each lens is adjustable by ± 3 mm along the beam direction for focusing and ± 1 mm in the perpendicular (x/y) plane. Adjustment is done by a single four-segment piezo tube operated in slip-stick motion (outer diam. 10 mm, inner diameter 9 mm, length 18 mm; supplier: Physik Instrumente, Germany). The direction of motion is controlled in a standard way by sign and amplitude of saw-tooth pulses applied to the four piezo segments with respect to the grounded inner electrode. The adjustment of the lenses with respect to the tip is thus simple and can be easily monitored by three low-cost digital cameras mounted outside the vacuum chamber at the end of each optical path. The aspherical lenses provide good light collection efficiency over the range of visible

wavelengths and a sufficient imaging quality with a wavelength-dependent resolution limit of 2-4 µm. This is an important result, as the manufacturer' design specification has a wavelength of 980 nm, which means that the aspheric shape has been optimized for wavelengths that are longer than those typically used in the types of experiments discussed here. The use of lenses (instead of mirrors) provides some achromaticity – discussed in the experimental part below. Moreover, glass lens and glass UHV viewports presently restrict the detectable light to the visible and near IR range.

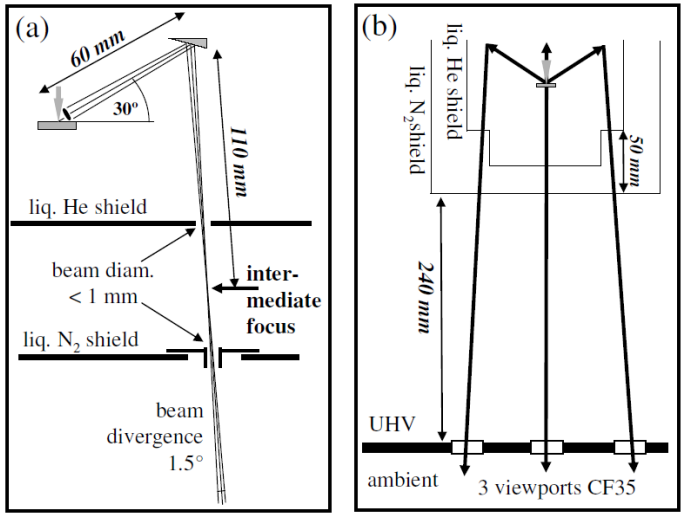

Figure 3.4. (a) Beam geometry of one of the three optical paths. For details of the beam passing through the two cryostat shields, see text. (b) Schematic cross section of the STM, the cryostat, and the bottom flange of the UHV chamber. The three beam paths are indicated by lines with arrows.

The three lenses couple light from the tunnel junction via three flat mirrors into three vertical light paths with the beams propagating in vacuum (Fig. 3.4 b). After passing through UHV viewports, the paths end outside the UHV chamber in three independent ports which can be employed in various combinations. Each port can be equipped with a web-camera (for lens adjustment), with an intensified camera, with a spectrometer, or with a single channel light detector (like e.g. a photomultiplier tube or avalanche photodetector). By reversing the propagation direction, light can also be coupled into each port providing directional illumination on the sample e.g. for photoluminescence experiments.

Most important for the further discussion of the optical set-up is the fact that the STM tip is fixed and all relative motion between tip and sample during coarse approach and during STM scanning is made by the sample. The lens units are attached to the same base as the tip holder, so that the relative adjustment of tip and lenses does not change by sample exchange and during STM operation.

3.2.3 The light path

The detailed geometry of the light paths is shown in Figs. 3.2-3.4. The entrance surface of the aspheric lens is typically adjusted to a distance of 2.5 mm from the tip apex. The lens focuses the light to an intermediate focus 170 mm behind the lens. From the lens the light passes inside the piezo tube (inner diam. 9 mm) and is reflected from an *ex situ* adjusted commercial silver mirror. The light exits the cryogenic part of the set-up through holes in the two radiation shields. The intermediate focus is situated between the inner radiation shield at liquid He temperature and the outer shield at liquid nitrogen temperature (Fig. 3.4 a). The focus prevents any blocking of the luminescence light by the holes, which act as apertures only when a wider area of the surface is imaged. The holes in the two radiation shields (diam. 4 mm in the liquid He shield and 6 mm in the liquid N_2 shield) reduce the thermal background radiation entering the STM. The negligible heat input into the 4.2 K system is reflected by the fact that the liquid He consumption remained unchanged comparing the situations before and after the holes were implemented into the shields. Calculation of the heat input assuming perfect black body radiation (ε=1) from the 300 K environment through a 28 mm^2 hole at a solid angle 2 msr yields an upper limit of the input power of 5 μW. The direct radiation on each lens (solid angle 0.4 msr) is less than 1 μW. This IR radiation is predominantly absorbed by the lens and only a minor part is transmitted to the tunnel junction.

The STM is firmly mounted on the liquid He tank which, however, is not rigidly attached to the liquid nitrogen tank, so that the relative alignment of the holes in the two radiation shields can change. In order to allow for adjustment, rather large holes were drilled into the liquid nitrogen shield. These holes are each covered by a plate containing a tube with a much smaller inner diameter (6 mm). Moving plate and tube from the outside of the UHV chamber by a wobble stick allows aligning the holes in the liquid nitrogen shield with the fixed holes in the liquid He shield (Fig. 3.4 a). After traversing the UHV viewports vertically (Fig. 3.4 b), the light from the tunnel junction is reflected by 90° to horizontal propagation and focused by a lens on the corresponding optical detector or camera.

3.2.4 Lens Adjustment by slip-stick motion

The *in situ* adjustment of the three lenses is a central point for the operation of the set-up. Lenses and motors are mounted on the liquid He tank and thus operated at 4.2 K in UHV. Under the standard focusing conditions described above a change of tip position by more than 50 µm requires lens re-adjustment to avoid losses at the holes in the cryogenic shields. *Ex situ* pre-adjustment of the STM tips on their mounts yields a reproducibility of only ≈300 µm. The fact that the exchange of an STM tip always requires a re-adjustment of the lenses emphasizes the importance of an easy-to-use *in situ* lens adjustment.

Fig. 3.3 shows one lens unit. Focusing of the lens (z-motion) is guided by two sapphire rods which act as rails. The motion is controlled by applying saw-tooth voltage pulses equally to the 4 piezo segments with respect to the inner grounded contact. Applying saw-tooth pulses with opposite signs to opposite segments leads to lateral (x, y) motion of the entire lens mount including the rails. The x/y plane of motion is defined by a sapphire plate whose surface normal is parallel to the light beam, i.e. tilted by 60° with respect to the direction of gravity. In order to compensate for the weight in the up/down motion, the lens mount base is pulled upwards by a wire attached to an appropriate counter weight.

Slip-stick motors require a controlled force normal to the contact surface. As the STM set-up does not feature coils for the generation of high magnetic fields, the normal force can be implemented by the magnetic force between permanent magnets and magnetizable steel. In other cases springs may serve the same purpose although the resulting normal force will change with the operation temperature, which might make operation less reliable.

3.2.5 Materials

The lens adjustment unit is composed of different materials that respond to specific requirements. The unit is made from UHV-compatible materials such as tantalum, sapphire, magnetizable and non-magnetizable steel, Al_2O_3 ceramics and others. In particular, $Co_{17}Sm_2$ magnets (supplier: Peter Welter GmbH & Co. KG, Germany) were employed to control normal forces in the slip-stick motors. The different parts are glued together by UHV-compatible conductive and non-conductive epoxy glues.

The optical properties of UHV components (e.g. the birefringence of UHV glass viewports) are rarely specified by manufacturers. Similarly, the UHV compatibility of commercial

optical components is in general not guaranteed and has to be tested prior to usage. We observed no significant outgassing at 100°C in vacuum for the aspheric lenses (uncoated precision molded aspheric lens, Corning C0550 glass, Light Path Technologies Inc., USA, supplier: Edmund Optics) and the plane mirrors (Ag protected coating ER.2 , Newport Corp.).

3.3 Examples of luminescence characterization

3.3.1 Monitoring the luminescence source

We employ low-cost web-cameras to monitor the tip approach. They are, however, not sensitive enough to detect the weak luminescence from the tunnel junction. This requires an intensified Peltier-cooled CCD camera to image the luminescence light spot and to picture immediately afterwards the tip and its reflection under illumination by an external light and at reduced intensifier voltage.
Fig. 3.5 c shows an overlay of such two images, allowing for an identification of the exact position of the tip apex. Fig. 3.5 b shows a plot of the CCD raw data without pixel binning and a cross section (red line above) through the maximum. This image of the luminescence from tip-induced plasmons demonstrates that the chosen aspheric lens is sufficient to obtain a spot with the dimension of a few pixels even at visible wavelengths.

3.3.2 Angular distribution of light emission

The use of free propagating beams (in contrast to a glass fiber guided coupling) allows preserving a maximum of information carried by the light. One such source of information is the angular distribution of emitted light which is only rarely monitored in STM-induced luminescence [69]. When the focus is purposely shifted away from the CCD plane, a broad spot is observed. This extended distribution represents the 2D Fourier transform of the waves composing the image of the light emitting point. It can be immediately interpreted as the angular distribution of the light emitted from the tip-sample region. The principle is illustrated in Fig. 3.5 a by the dashed and the dotted beam propagating at some angle with respect to the optical axis. Fig. 3.5 d shows the angular distribution obtained in the Fourier-transforming geometry in one of the light paths.

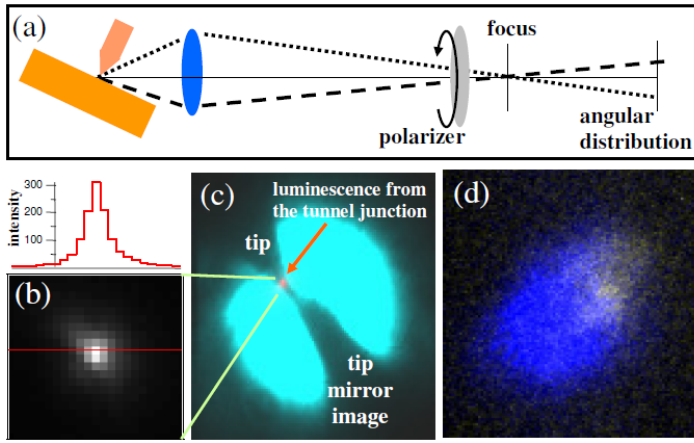

Figure 3.5. (a) Schematic geometry of polarization and angular distribution measurements. Image of tunnel junction and luminescence light source: (b) focal image (below) and cross section (red line, above) of the intensity distribution of the light emitted by tip-induced plasmons. (c) Overlay of the luminescence focal image (red) with the shadow image of the tip and its mirror image illuminated from the back (cyan). (d) Overlay of the angular distributions of the component polarized along the surface normal (p-polarization, blue) and the perpendicular component (s-polarization, green). The yellow region indicates roughly identical intensities of the two polarizations.

Our example maps the anisotropy found in the emission from tip-induced surface plasmons on a metallic sample (s. Fig. 3.5 d). We discuss the color-coding in this figure in the next section. The deviation from the circular shape demonstrates that the anisotropy of light emission in the azimuthal direction is less pronounced than the anisotropy found for different elevation angles. The tip-sample orientation in Fig. 3.5 d is the same as in Fig. 3.5 c. The measurable azimuthal emission distribution can in principle be extended further by including the information from the other two lenses. We observed that the intensity from tip-induced plasmons in the three light paths can vary significantly. As the three paths are almost identical by design, we ascribe this observation to the irregularity of the tip apex and the resulting differences in the coupling of tip-induced plasmons to the emitted far field [71]. We have not yet investigated angular information for light sources other than tip-induced plasmons. However, we suggest that the observation of angular luminescence distributions can contribute to the characterization of anisotropic emitters like, e.g. quantum wires or luminescent molecules. The identification of nodes in the angular distribution allows an assignment of the orientation

of the local transition dipole which has been introduced by far-field microscopy studies of single molecules [72,73].

3.3.3 Polarization analysis of luminescence

The information obtained by the angular distribution of luminescence can be supplemented by polarization analysis. Fig. 3.6 a shows a polar plot of the integrated light intensity from one lens as a function of polarizer angle. The data (red dots) were fitted (blue line) by a sum of two components, an isotropic one (green line) and a dipolar one (red line).

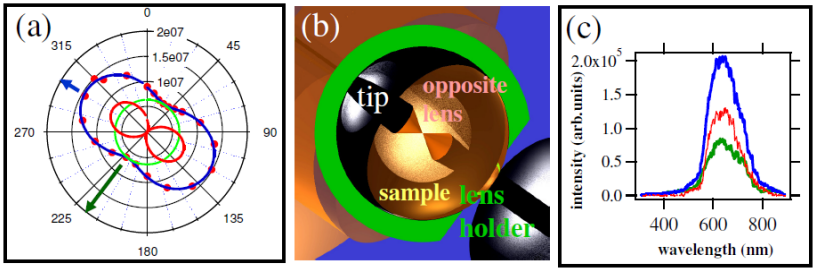

Figure 3.6. (a) Polar plot of the polarization-dependent spectrally-integrated for emission from tip-induced plasmons. (b) Simulation of tip-sample geometry for the measurements in (a). (c) Spectra recorded along the two principle axes of linear polarization. The color coding is the same as in the polar plot (a). From single photon calibration an estimate of absolute photon numbers is obtained by dividing the arbitrary units by 50.

The result clearly indicates a dominant direction of the electric field vector in the radiation. As the direction of observation is not identical to the one in Fig. 3.5 c, d, the apparent orientation of the surface normal is different. We employ a realistic visual simulation of the 3D geometry (software: POV-Ray (TM) for Windows, Version 3.5) which reproduces realistically the actual view into one of the viewports. The simulated view towards the aspheric lens (Fig. 3.6 b) allows determining the projection angle of the coordinates in the STM and proves that the preferential polarization of the tip-induced plasmons is parallel to the surface normal (p-polarization). This may appear obvious when regarding the electric field associated with the tip-induced plasmon. It might be more surprising that the component polarized parallel to the surface (s-polarization) is comparable in intensity to the p-polarized contribution (red line). The use of a quarter wave plate can additionally determine the

circularly polarized component. A full polarization analysis has been discussed by Pierce *et al.* [74]. The spectra in the direction of maximum intensity (blue) and minimum intensity (green) are plotted in Fig. 3.6 c together with the difference of the two spectra (red) with the color coding equivalent to the polar plot in Fig. 3.6 a. The two linear polarization components show no significant spectral difference. Finally, we demonstrate the measurement of the polarization-resolved angular distribution by combining Fourier imaging (see previous section) with polarization analysis. Fig. 3.5 d is a color coded overlay of the polarized contribution and the non-polarized contribution (blue and yellow, respectively). It is remarkable that the s-polarized contribution varies strongly with the azimuth of emission. This supports the assignment to tip apex irregularities suggested in the previous section.

3.3.4 Spatial luminescence mapping and tunneling excitation spectroscopy

Fig. 3.7 demonstrates the ability to record a map of the total emitted light intensity in STM scanning mode. The luminescence image was recorded during a 30 minute topography scan (512 x 512 pixel, current 0.5 nA). The short charge pulses (< 1 µs) from the single channel detector, here a photomultiplier tube (PMT), were integrated by a commercial measuring amplifier (DC-1000, Alexander Meier Elektronik, Germany) with the band width reduced to 10 Hz. This low pass filtered signal is then fed to a separate input channel of the STM scanning electronics.

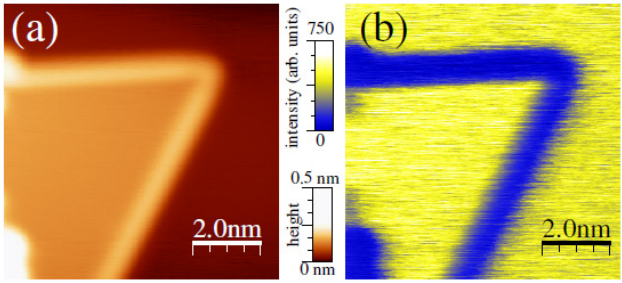

Figure 3.7. (a) Topographic scan with a simultaneous acquisition of (b) luminescence intensity. Ag coated W tip on Ag(111), bias U = 3.0 V, tunnel current I = 0.5 nA, 512 x 512 data points, scanning speed 1.8 s per line. Band width of luminescence channel 10 Hz. The plots were made using WSxM [75] software.

The observed reduction of luminescence intensity near step edges with respect to terraces has been discussed earlier [76,77]. In our measurement it can be related to an increased tip-sample distance shown by the bright edges in the topographic image. The tip retraction is not a dynamic effect from the STMs feed-back at the step-edge because the same behavior is observed for step edges parallel and perpendicular to the scanning direction. It can be due to a reduced tunnel barrier or an increased density of states.

In the same way as in topographic scans one can record bias-dependent luminescence synchronously with the acquisition of tunnel current and differential resistance (dI/dV data from a lock-in amplifier). Fig. 3.8 shows examples for a single forward and backward bias sweep acquired within 20 s.

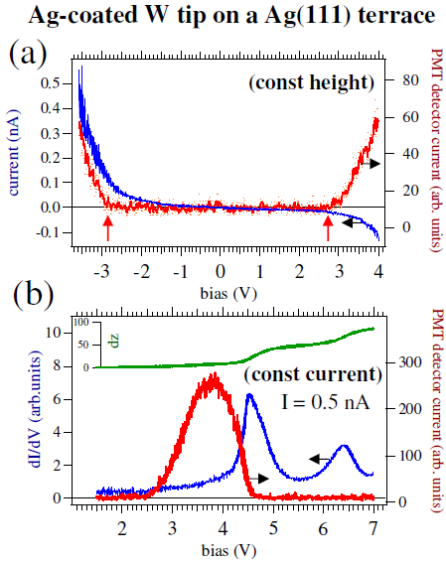

Figure 3.8. Tunneling spectroscopy (I and dI/dV: blue traces) with simultaneous recording of total luminescence intensity using a PMT (red trace) for a Ag coated W tip on Ag(111). Single forward and backward bias scan at 10 s per sweep. Band width of luminescence channel 10 Hz. (a) Constant height mode, set point V = –3.6 V, I = 0.5 nA. (b) Constant current mode, I = 0.5 nA. Green trace: Height change of the STM tip during bias sweep.

Recording this type of excitation spectrum at a constant height condition (Fig. 3.8 a) yields the light emission onset at both polarities - here at similar absolute voltages (red arrows). This is due to the fact that with few exceptions [78,54] a photon is not found to carry more energy than

provided by a single tunneling charge. The photon generation efficiency can be obtained by dividing the light intensity (red curve in Fig. 3.8 a) by the current (blue curve). This ratio can be obtained directly, and with higher precision, in a constant current measurement as in Fig. 3.8 b. The decrease of the quantum efficiency above 4 V may in part be due to the retraction of the tip from the surface (green curve) which occurs in response to an increased conductance due to the upcoming first field ionization resonance at 4.5 V. As the tip-induced light emission requires the proximity of tip and surface, a tip retraction leads to a reduction of the light emission [42].

3.3.5 Chromatic aberration in luminescence spectra

An important type of measurement which contains rich information on the studied photon source is light spectroscopy at a previously characterized surface position. We present as an example spectra recorded with a W tip on a terrace of a Cu(110) single crystal. In Fig. 3.9, the light intensity is plotted in a reverse rainbow color scale as a function of bias voltage (y-axis) and wavelength (x-axis). This plot is overlaid with contour lines of constant light intensity. The plot is composed of single plasmon spectra with a total accumulation time of 2.7 hours and provides an overview of the relation between excitation energy (bias voltage) and emission energy (plasmon wavelength). We note that for the constant current condition the bias voltage is connected with the tip-sample distance in a monotonic but not linear relation. For an increasing voltage, the light intensity at a given wavelength does not show a linear increase, but exhibits subsequent maxima and minima. The reason for that is the non-linear change in tip-sample distance, which affects the strength of the tip-induced plasmon modes, as well as the probability of inelastic tunneling [79].

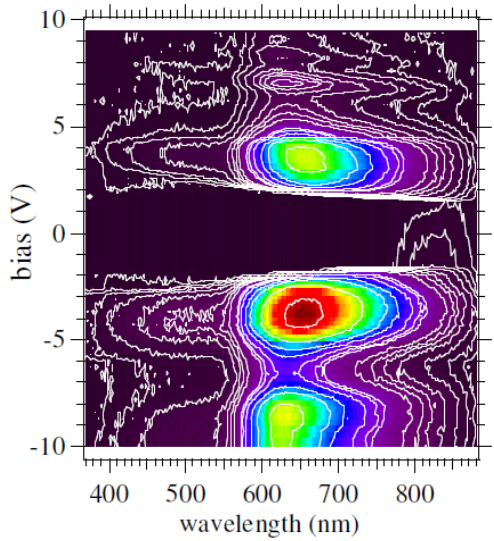

Figure 3.9. "Fingerprint" measurement of tip-induced plasmon polaritons for a W tip on an atomically flat terrace on Cu(110). The 76 separate spectra recorded with a tunnel current I = 1 nA for different bias voltage (y-scale) are presented in a color coded 2D intensity plot together with white contour lines of equal intensity (the intensities for which the contour lines are drawn are arbitrarily chosen).

A prerequisite of detailed spectroscopic data is a high resolution of the imaging optics. In order to reduce losses, we operate the spectrometer with a wide entrance slit. Fig. 3.10 shows a false color (reverse rainbow) representation of the pixel-wise read-out from the CCD chip at the spectrograph. Such data is the basis for the generation of spectra. The broad spectral distribution of tip-induced plasmon emission in this example allows the visualization of a bow-tie shaped pattern in Fig. 3.10. The focus obtained at the center is comparable to the diameter of the radiation source image in Fig. 3.5 b. The broadening towards the sides of the spectrum can be attributed to the chromaticity of the aspheric lens in our set-up. Changing the focus in the spectrometer allows shifting the center of the bow-tie to higher or lower wavelengths. Conventionally integrated spectra obtained from the CCD array thus achieve the instruments limiting spectral resolution only over a restricted wavelength range. If a larger range is to be covered, the spectra have to be measured for every wavelength interval at a different focal setting of the imaging lens outside the UHV chamber. Alternatively, the data from the CCD array can be deconvoluted by a wavelength-dependent broadening.

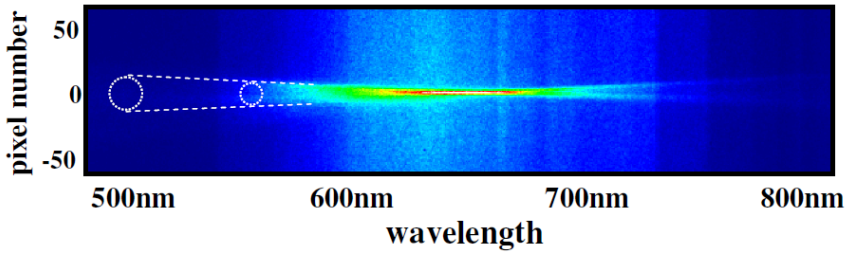

Figure 3.10. Spectroscopic CCD raw data (1024 x 256 pixels) in false color representation characterizing the chromatic aberration of the optical system (see text).

3.3.6 Outlook

Further opportunities for other measurements are opened by the simultaneous use of the three optical ports: First, light can be coupled into the tunnel junction through one port, allowing for photoluminescence measurements, with the STM tip either removed or in place. Focal spots down to 3 µm may be achievable. The field enhancement in the presence of the metallic tip will increase the spatial confinement of incoming light to dimensions near the curvature of the tip apex (10-50 nm) similar as in apertureless near-field optical microscopes (a-SNOMs). Second, one can imagine equipping two optical ports each with a time-resolving photon detector. Fast processes induced by the STM tunnel current can thus become accessible via time correlation measurements. This technique will be described in Chapter 7.

4 Single pentacene molecules on ultrathin insulator films

Organic molecules deposited on a metal surface are known to interact through their π-orbitals with the free electron gas at the metal surface. This can lead to a charge transfer with [80] or without [81] a chemical reaction between metal and molecule. In order to avoid such interactions, an insulating spacer layer with a large band gap (several eV) can be used, which acts as a tunnel barrier towards the metal. Repp *et al*. showed in an STM study that 1 to 3 atomic monolayers of NaCl already provide a sufficient electronic decoupling of pentacene from the metal surface of Cu(111) [22]. The molecule undergoes no reaction with the inert NaCl, demonstrated by the observation of the unperturbed gas-phase like frontier orbitals of pentacene on this substrate.

Here we used ultrathin insulating layers of KCl and the h-BN-nanomesh, which have a large bandgap (8.4 eV for bulk KCl, 5.9 eV for h-BN), in combination with different metal surfaces as templates for pentacene. The electronic properties and by this the interaction between the molecules and the substrate are revealed by a combined STM and STS study on individual pentacene molecules. We find that the insulating properties of the buffer layer are not alone provided by the material, that is, by its chemical composition. A significant role is played by the underlying metal and its crystal face, which determine the structure of the insulator [82, 57] and, as we will show in detail, the electronic properties of the molecule. We obtain a good electronic decoupling of pentacene on the close packed metal surfaces, i.e. for KCl/Cu(111) and KCl/Au(111), whereas on KCl/Cu(110) a strong molecule substrate interaction takes place resulting in a poor electronic decoupling.

4.1 The insulators

KCl is thermally evaporated and partially covers the underlying substrate. KCl grows in a carpet-like mode [83] over the step edges (s. Fig 4.1 a). On top of the wetting layer KCl forms islands with straight edges. The islands are homogeneously distributed and also show a carpet-like growth over the step edges. The first KCl wetting layer on Au(111) consists of two

monolayers of KCl. The wetting layer shows a step-height of 4 Å being larger by a factor of two than the step height of the islands formed on top of it (Fig. 4.1 a). The lattice constant of bulk KCl is 6.29 Å [84]. The KCl double-layer perpendicular to the (100) plane has thus a thickness of 3.15 Å. In the STM the apparent height of the first step is larger than expected from the lattice constant. Similar to KCl, the wetting layer of the bilayer of NaCl on Cu(111) measures a larger step height of 3.2 Å [85], which agrees well to our results, taking into account the smaller lattice constant of NaCl (5.65 Å). The surface corrugation observed on the KCl layer results from the Au(111) reconstruction still visible even through the 3rd KCl layer (Fig. 4.1 a).

In the case of KCl deposition on Cu (s. Fig. 4.1 b, c, d), the KCl surface exhibits a striped corrugation due to the formation of a Moire pattern resulting from the lattice mismatch between KCl and the metal [56]. On Cu(111) a single phase was observed with Moire-stripes oriented along the three symmetry directions of the (111) surface. As for KCl on Au(111), the KCl wetting layer on Cu(111) is a bilayer, on top of which monolayer-islands form [86]. When evaporated on Cu(110), KCl exhibits two different phases called type I and type II, both of them also show a striped Moire structure (s. Fig. 4.1 b, c). The stripes of type I are oriented parallel to the [-110], whereas the type II stripes are parallel to the [-112] direction of the Cu(110) surface [56]. In contrast to Au(111), the apparent step heights of KCl type I and II measure a step height of 2 Å (at a bias of -3V) [56] for the wetting layer, which compares well with the measured height of the monolayer islands on Au(111). This suggests that the KCl wetting layer on Cu(110) is a monolayer [56]. The KCl phases formed on the Cu(110) and Cu(111) differ substantially with respect to the corrugation height of their Moire-patterns. In Fig. 4.1 the surface structure is shown. The observed periodicities in comparison to the bulk lattice constant of KCl indicate that only one chemical species in the KCl layer is imaged by STM as a protrusion. In analogy to studies of NaCl ultrathin layers, we assume that the Cl ions appear as protrusions [87]. The KCl-type I structure forming on Cu(110) exhibits the strongest corrugation which is 6 times larger than the KCl phase on Cu(111). For a detailed description of the KCl-morphology on Cu(110) and Cu(111) the reader is referred to [56, 86].

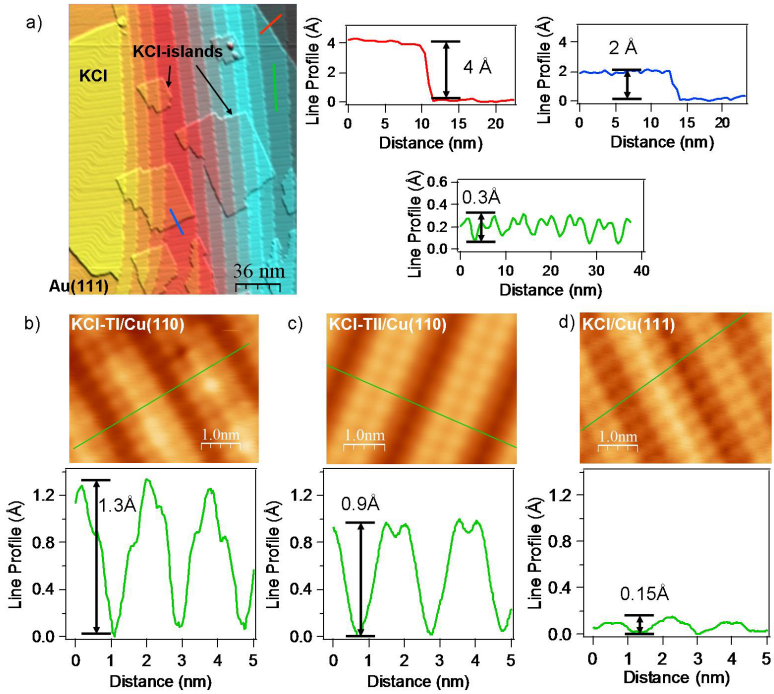

Figure 4.1. (a) STM-topographs of KCl/Au(111), (-3 V,0.01 nA) and line-profiles showing the step heights of the first (red) and the second KCl-layer (blue). The green curve shows the surface corrugation of KCl/Au(111). (b),(c),(d): High-resolution topographs (upper row) and corresponding line-profile (lower row) of the KCl/metal systems (b): KCl-typeI/Cu(110), (-0.47 V,0.1 nA); (c): KCl-typeII/Cu(110),(-1.7 V,0.2 nA), (d): KCl/Cu(111), (2 V,0.05 nA).

The boron nitride monolayer was prepared by a high-temperature exposure of the clean rhodium surface to borazine $(HBNH)_3$, as described in Chapter 3.1.2. It forms a hexagonal superstructure with a periodicity of 3.2 nm, a 2 nm pore size and covers the metal surface continuously. Pore-formation is due to the lattice mismatch of the film and the rhodium substrate. The pores are periodic depressions of the layer (s. Fig. 4.2 b) and act as traps for atomic or molecular adsorbates [88].

4.2 Electronic properties of pentacene deposited on the insulator-metal substrates

An STM study on individual pentacene molecules adsorbed in a planar geometry on a NaCl layer on Cu(111) have been reported by Repp *et al.* [22]. The authors observed the highest occupied (HOMO) and lowest unoccupied (LUMO) molecular orbitals of pentacene imaged by the STM at opposite bias polarities. Tunneling through the HOMO or LUMO results in a charging of the molecule, thus the observed states are more accurately referred to as the positive (PIR) and negative (NIR) ion resonances, respectively. The geometries of both orbitals are clearly distinguishable. The HOMO orbital exhibits 10 lobes of the electron wave function ordered in two rows separated by a nodal plane along the long axis, whereas the LUMO shows 7 lobes and no nodal plane along the long axis. The voltage difference between the PIR and NIR is 3.1, 3.3 and 4.2 eV for a pentacene molecule on a mono-, bi- and triple-layer of NaCl, respectively [22]. The increase of the NIR-PIR-gap from a mono to a triple layer of NaCl was attributed to the decrease of polarization by the metal surface due to the larger molecule-metal separation for the thicker layers. In this work we explore different insulator-metal combinations in order to gain information on the influence of the substrate systems on the molecular level alignment of pentacene molecules and by this to study the electronic decoupling introduced by the insulators. We will discuss three different models for a description of the strong molecule-substrate interactions in the system pentacene-KCl-Cu(110).

Samples were prepared by thermal evaporation of pentacene on thin insulator films on metal substrates. When pentacene is deposited on the KCl-covered metal surface held at room temperature, the molecules accumulated exclusively on those regions which were uncovered by KCl. A suitable approach to reduce the diffusion path length of pentacene on the KCl was cooling of the substrate to 90 K during the molecule deposition. Thus we obtained isolated pentacene molecules with a preferential adsorption site in the channels between the KCl-stripes (Fig. 4.2 a, c). In contrast, isolated molecules are found on the BN-nanomesh even at room temperature because the areas between the pores act as diffusion barriers (Fig. 4.2 b) and BN covers the metal surface completely. The molecules are found preferentially at the edges of the pores. This characteristic adsorption site was already observed for CuPc/BN/Rh(111) and has been assigned to the position with the highest in-plane electric field on the surface [88].

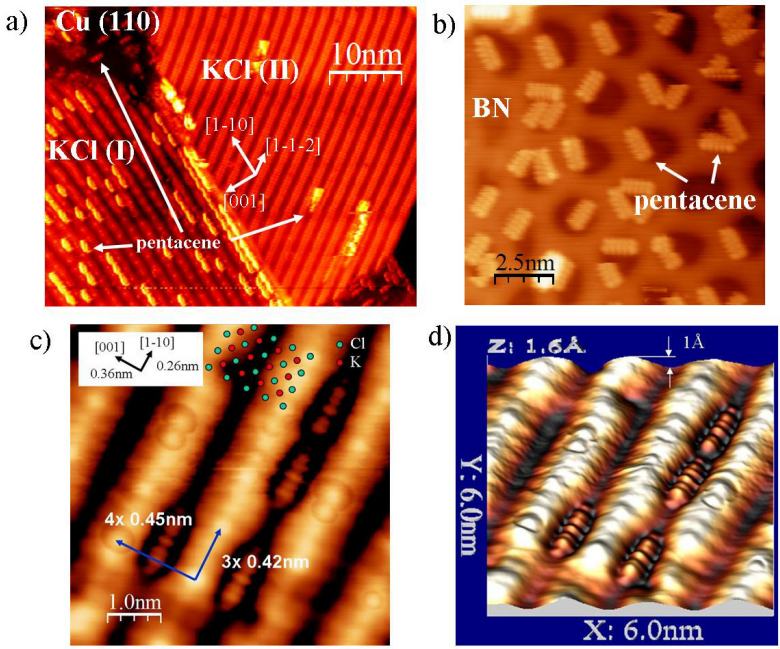

Figure 4.2. STM topography overview, (a) pentacene on bare Cu(110) and on single layers of KCl type I and II on Cu(110) (U = -0.5 V, I = 5 pA, (b) pentacene adsorbed on a BN-nanomesh (U = -2.15 V,I = 0.2 nA), (c) adsorption geometry of pentacene and lattice assignment of the ions in KCl-type I (U = -0.1 V, I = 0.3 nA), $d_{Cl\text{-}Cl} = a_{KCl}/\sqrt{2} = 0.45$ nm, d) 3-dim representation of the same measurement as c).

The samples were characterized by imaging the topography with the STM and spectroscopy. The topography measurements were done in the constant current mode of the STM, current-voltage spectroscopy was performed by measuring the differential conductance by the lock-in technique with a voltage modulation of 20 mV amplitude and a frequency of 750 Hz. Differential-conductance maps were taken by recording the lock-in signal during the scan in the constant current mode.

Spectroscopy measurements on single pentacene molecules reveal one peak at negative and one at positive bias. In all measurements the bias is the sample potential with respect to the tip potential. The voltage difference between the peaks ranges from 1.5 V to 4.2 V for the different substrate systems (s. Fig 4.3). Except for the case of pentacene on KCl-type I/Cu(110) the voltage gap between the observed peaks are close to the result

reported for the NaCl/Cu(111) substrate [22]. Topographs of the molecule at bias voltages corresponding to the peaks reproduce the pattern of the lowest unoccupied (LUMO) and highest occupied (HOMO) molecular orbital of the free molecule (s. Fig. 4.3 a): KCl/Au(111) and b): h-BN/Rh(111)). When imaged at a bias voltage within the NIR-PIR gap the molecule appears featureless and with a low topographic height (see Fig. 4.2 b, scan at -0.6 V). The orbitals of the free pentacene molecule are preserved when it is deposited on the BN or KCl on Rh(111) and Au(111) respectively (Fig. 4.3 a,b).

In the case of pentacene on KCl-type I / Cu(110), the bias difference between the STS peaks is by a factor of 2 smaller than for the other template systems. dI/dV-maps show the same geometry as the LUMO orbital of the free molecule on both sides of the Fermi-level (s. Fig. 4.3 c). This observation differs from the other insulator/metal systems in Fig. 4.3 where the pentacene LUMO orbital is accessed always at positive bias. The observation of the LUMO-orbital at an energy below the surface Fermi-level suggests that the LUMO-state might be populated either partially (by 1 electron) or fully (by 2 electrons). Both indicate that a charge transfer to the pentacene takes place. STM-topographs of pentacene on the KCl-type II phase reveal the geometry of the LUMO orbital at 0.5 V. The orbital shape appears slightly bent in the direction of its long axis. This indicates that the adsorption site is not mirror symmetric. Unfortunately, at negative bias (-2.3 V) the STM topography of pentacene on the type II structure does not show the molecular structure in detail (Fig. 4.3 d). High-resolution STM imaging of pentacene in this voltage range was hampered by the molecules' high mobility on the type II phase, which is induced during scanning by the electric field of the tip. The high mobility of pentacene on both KCl/Cu(110) phases does not indicate a strong bonding to KCl. However, pentacene is significantly more stable (against motion by the electric field of the STM tip) on KCl-type I/Cu(110) than on KCl/Cu(111). In addition, the corrugation of adsorption potential, that is, the diffusion barrier on the type I phase, is higher than for type II. This results in a higher pentacene-coverage on type I (s. Fig. 4.2), whereas the imaging on type II is unstable. The different mobilities of pentacene might be further related to the topographic corrugation of the KCl (Fig. 4.1), which is the highest for the KCl-type I-phase.

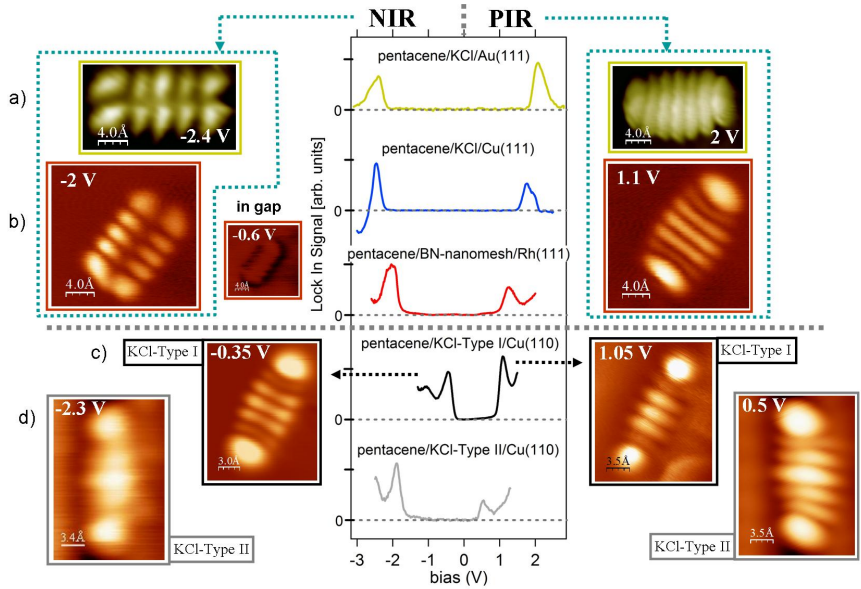

Figure 4.3. Scanning Tunneling Spectroscopy STS (center) and bias-dependent imaging (right, left) of individual pentacene molecules on different insulator/metal systems. The spectra are offset in vertical axis for clarity. The grey dotted line separates schematically the systems with good (top) and poor (bottom) electronic decoupling. Images: individual pentacene molecules on (a):KCl/Au (yellow, STM-topography), (b): BN/Rh(111) (red, dI/dV-map), (c): KCl-type I/Cu(110) (black, dI/dV-map), (d): KCl-type II/Cu(110) (grey, STM-topography).

In one case the observation of identical molecular states on both sides of the bias polarity was reported for CuPc on ultrathin oxide layer on NiAl [89]. In another case such an observation was attributed to singly occupied molecular orbital formation by pentacene reacted with a Au atom [90]. We will start the discussion with the first case.

The voltage drops in the double tunneling barrier between the vacuum gap on one side and the insulator on the other side of the CuPc molecule. The current can flow for different polarities through the same molecular level, if it can align for one polarity with the Fermi level of the tip and for the opposite polarity with the Fermi level of the metal substrate. This requires that the molecular level is not pinned to the metallic substrate, i.e. the insulator provides a sufficiently large voltage drop [89].

In order to obtain information about the shift of the pentacene levels in the double barrier STM junction between vacuum and the KCl-type I/Cu(110), we performed dI/dV spectroscopy at varying tip-sample separations (s. Fig. 4.4 a). Each spectrum was taken at a fixed tip-sample distance. A total range of 1.7 Å could be covered. In Fig. 4.4 b the corresponding peak positions of the peak B_2 at positive bias (blue) and the peak B_1 at negative bias (red) are plotted for all spectra as a function of relative tip-sample distance change *dz*. Both peaks obtain linear shifts S_1 and S_2, which denote the peak energy change *dE* as a function of tip-sample distance change *dz*. The peaks shift towards smaller absolute energies with increasing electric field, i.e. at smaller tip-sample separations.

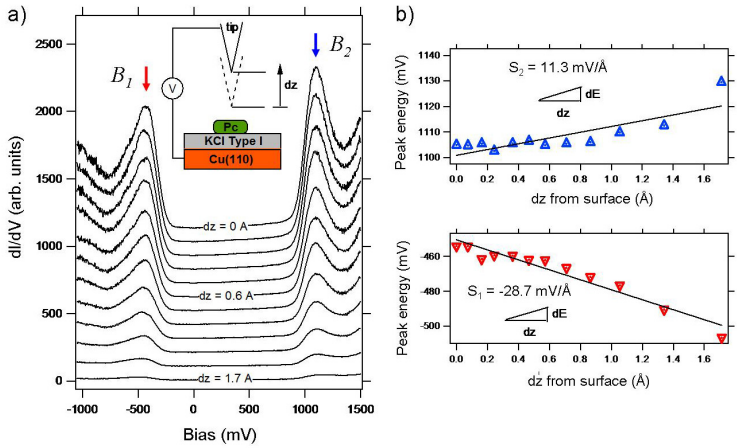

Figure 4.4. (a) Spectroscopy at varying tip-sample distances on pentacene deposited on KCl-type I/Cu(110). (b) Shifts S_1 and S_2 of the peaks B_1 (below) and B_2 (above) with relative tip-sample distance *dz*.

Wu *et al.* proposed a model describing the case of bipolar tunneling through the same molecular level based on electrostatics [89]. According to this model, the observed peak positions B_1 and B_2 measured in eV and the original position E_0 (eV) of the state with respect to the Fermi level without biasing the junction are related, as follows:

$$B_1 = E_0\left[1 + d/\varepsilon z\right], \tag{4.1}$$

and

$$B_2 = -E_0\left[1 + \varepsilon z/d\right]. \tag{4.2}$$

Here, ε is the dielectric constant of the insulator, d is the insulator thickness and z the tip-molecule separation. When the tip sample separation z and thus the electric field across the junction changes, the observed orbital energies shift by the electrostatic voltage drop. According to the model, the peak-shifts S_1 and S_2 upon change of z are related by:

$$\frac{S_1}{S_2} = \left(\frac{d}{\varepsilon z}\right)^2 > 0\,, \tag{4.3}$$

When the model is applied to the tunneling through a CuPc molecule on Al_2O_3/NiAl, the peaks shift in the same direction related to the bias scale, and the shift-direction is defined by the sign of E_0.

By setting the peak positions of pentacene to B_1=-0.45 eV, B_2=1.10 eV (read out from the spectrum for dz=0) and putting it in (4.1) and (4.2)), we obtain E_0=-B_1*B_2/(B_1-B_2)=-0.32 eV, which means that the true position of the state is below the Fermi level of the substrate, thus the pentacene would be negatively charged. However, for the ratio of the measured peak shifts we obtain $S1/S2$=11.3(meV/Å)/-28.7(meV/Å)=-0.4, a value smaller than 0, because the peaks of pentacene shift in opposite directions in contrast to the model of Wu *et al*. Moreover, the absolute value of the shift S_2 is expected to be larger than S_1 by a factor of $(\varepsilon z/d)^2$ (eq. 4.3). With $\varepsilon_{(KCl)} \approx 4.8$ *and* $z \approx d$, the shift S_2 of peak B_2 should be one order of magnitude larger than the measured one. From these results we conclude that our data is incompatible with the model and that the observed electronic features of pentacene on KCl-type I/Cu(110) do not result from bipolar tunneling through the same level.

If we assume that the LUMO of pentacene is originally filled by one electron, a further process is possible. By applying a negative bias (-0.5 V), this orbital could be emptied, whereas at +1.1 V a second electron could be injected into the same state. Such a configuration was reported for a 6-gold-pentacene complex on NaCl/Cu(111) [90]. Due to the bond formation between a gold atom and a pentacene molecule an electronic configuration results, for which the complex obtains a singly occupied molecular orbital (SOMO). The authors observed the same orbital geometry of the SOMO at both bias polarities. In this case the energy difference between both peaks is a direct measure for the Coulomb energy needed for an adding/removing an electron to/from the same orbital of the complex. However, the energy difference between the SOMO peaks of the 6-gold-pentacene complex is substantially higher (2.7 eV) compared to the gap energy between the peaks B_1 and B_2 in Fig. 4.4. In our case pentacene can interact only with the surface, thus a charge transfer from KCl/Cu(110) has to take place, which would be energetically unfavourable for a free standing pentacene molecule. The negative charge on pentacene might be stabilized due to the specific

arrangement of the K^+ and Cl^- ions at the adsorbtion site (s. Fig 4.2 c, d). This might also have an impact on the observed smaller peak distance between B_1 and B_2 in comparison to the SOMO gap of the 6-gold-pentacene complex. In order to describe such charge stabilisation on the molecule due to the surface, a theoretical model would be required that includes a description of the electronic properties of the KCl-type I-layer, the strong corrugation amplitude (s. Fig. 4.1 c) as well as the electrostatic surface potential at the pentacene adsorption site.

Unlike KCl on Cu(111) and Au(111), type I phase on Cu(110) might have electronic properties strongly deviating compared to the bulk phase. In Fig. 4.5 a comparison of the dI/dV spectroscopy taken on pentacene and on the KCl-type I on Cu(110) is shown. The conductivity on KCl vanishes in a very small bias range between -400 mV and 200 mV. We obtain an increased conductivity at higher voltages, that is strongly pronounced in particular above 800 mV and extending in the region of the pentacene peak at + 1100 meV.

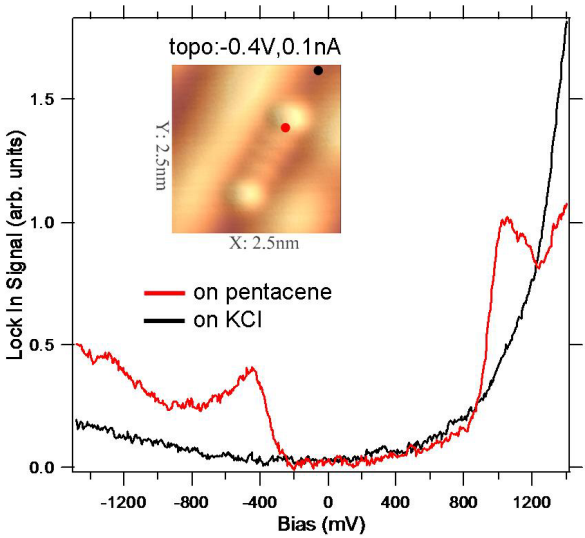

Figure 4.5. Scanning Tunneling Spectroscopy (STS). A comparison between pentacene/KCl type I/Cu(110) and KCl type I/Cu(110).

The spectroscopy on KCl type I shows a non-vanishing background of density of electronic states, indicating that the band gap of the KCl is not fully developed. Thus, the insulating properties of KCl type I are substantially reduced. This leads to a third model to describe the

electronic properties of pentacene/KCl type I/Cu(110). Molecule-substrate interactions might result in weak hybridization of pentacene states with the states of the metal substrate and the formation of new molecular states as reported for pentacene on Cu(110) by Yamane *et al.* [91]. The authors suggest a formation of an interface state deduced from the hybridization of the molecular orbitals with the Cu(110) surface with a possible modification of the orbital symmetry. Although the interaction of pentacene with an underlying metal is much stronger than the interaction with the metal through the type I KCl layer, the increased conductivity (s. Fig. 4.5) obtained on the KCl suggests that electronic hybridization may have to be taken into account.

4.3 Work function of the ultrathin insulators

The observation of gas-phase molecular orbitals of pentacene on BN/Rh(111) and KCl on close-packed noble metals, as well as NaCl/Cu(111) [22] suggest that the molecule substrate interaction is low. Repp *et al.* compares the relative positions of the molecular states to the corresponding work function of the substrate. It turns out that the molecular levels align according to a common vacuum level of pentacene and the substrate. It follows that the NIR/PIR state, i.e. the injection barriers for electrons/holes at the molecule–substrate interface, are determined by the difference between the work function of the substrate and the electron affinity/ionization potential EA/IP of the organic molecule. The equivalent situation for organic solids is known as the Schottky-Mott rule. It is expected to hold if there is no interaction between the metal and the organic semiconductor [81]. If the work function of the substrate is comparable or even smaller than the electron affinity of the adsorbate, a charge transfer to the molecule will occur. In order to investigate how well this rule applies in the case of pentacene molecules on KCl we measured the work function differences of the metal substrate and the KCl covered metals.

The measurements are done by recording the current as a function of tip-sample distance z (described in section 2.2), which is linearly ramped over a range of 3 Å. The bias voltage is kept constant at 0.1 V. Due to the decrease of the tunneling gap, the current increases exponentially over approximately three orders of magnitude (s. Fig. 4.6). In order to exclude spurious results due to tip changes we did subsequent measurements on the clean metal surface and the KCl-phase. The evaluation of the measurements follows eq. (2.9), which gives the mean work function between tip and surface. However, if the difference of work functions

is taken between the clean and KCl-covered surface for an identical tip, the unknown work function of the tip cancels out.

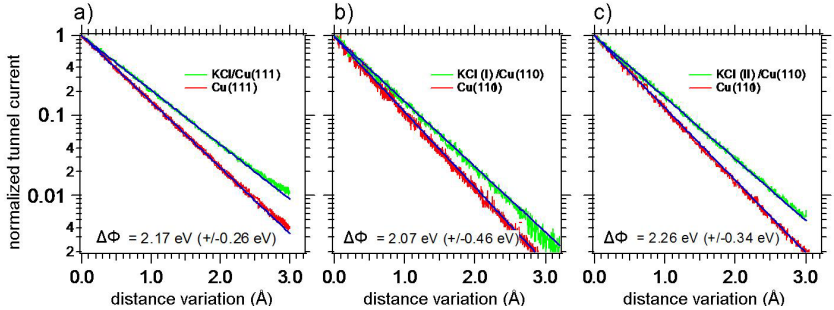

Figure 4.6. Logarithmic plot of the I(z) measurements for (a) KCl/Cu(111), (b) KCl-type I/Cu(110), (c) KCl-type II/Cu(110). The fits (black) are done according to eq. (2.9) and yield the difference ΔΦ (absolute value) of the mean work function between the metal and the KCl/metal surface. The smaller absolute slope of I(z) measured on KCl results in a smaller mean work function compared to the clean metal surfaces.

In the difference there remains a minor contribution of the image potential difference between metal and salt layer. As the dielectric constant of the salt is larger than for the metal, the obtained work function difference is a lower limit compared to the real value. Table 4.1 gives an overview on the work functions (WF) of the clean and KCl-covered metal surfaces. The WF-difference ΔΦ measured between the clean and the KCl-covered metal surfaces is substracted from the known WF_M of the corresponding metals from literature. In this way, the WF_{KCl} of the KCl-covered metal surfaces is obtained.

Table 4.1 Work functions of the clean and KCl-covered metal surfaces.

metal surface	measured mean WF-difference ΔΦ (eV) between metal and KCl/metal	WF_M (eV) of the bare metal surface [92]	calculated WF_{KCl} (eV) for KCl/metal $WF_{KCl}=WF_M-\Delta\Phi$
Au(111)	-1.63±0.50	5.4	3.8
Cu(111)	-2.17±0.26 (Fig. 4.6a)	4.9	2.7
Cu(110)	-2.07±0.46 (type I) (Fig. 4.6b)	4.5	2.4
Cu(110)	-2.26±0.34 (type II) (Fig. 4.6c)	4.5	2.2

It is apparent that the metal work function is more strongly reduced for the KCl layer (ΔΦ ranging between 1.6 and 2.2 eV) than for the NaCl (approx. 1.1eV) [93,94]. Table 4.2 shows the data of pentacene spectroscopy (Fig. 4.3) and the substrate work functions (Table 4.1). If

the molecule-substrate interaction is negligible, the difference between work function and NIR level should be constant.

Table 4.2 Work functions and molecular level positions for pentacene/KCl/metal.

orbital energy (eV)	PIR (V)	NIR (V)	WF_{KCl} – NIR (eV)	NIR – PIR (eV)
KCl/Au(111)	-2.4	+2.1	3.8-2.1 = 1.7	4.5
KCl/Cu(111)	-2.5	+1.8	2.7-1.8 = 0.9	4.3
KCl (I) /Cu(110)	-0.5	+1.1	2.4-1.1 = 1.3	1.6
KCl (II) /Cu(110)	-1.9	+0.7	2.2-0.7 = 1.5	2.6
electron affinity EA (eV) of pentacene [95]			1.35	

In fact, the difference between the WF_{KCl} and NIR of pentacene, shows a reasonable agreement with the electron affinity (EA) of pentacene. The work function is always larger than the electron affinity of pentacene and according to the common-vacuum level alignment this gives the energy needed for charge injection, which is represented by the position of the NIR. As already discussed above, the measured value of the work function can not explain a charging of pentacene on the KCl-type I/Cu(110). The observed differences between NIR-PIR of pentacene KCl/Cu(111) and KCl/Au(111) are in a good agreement with the NIR-PIR gap observed on a bilayer of NaCl on Cu(111) reported by Repp *et al*. Additionally, the frontier orbitals of pentacene on BN as well as KCl on close-packed metal surfaces are well preserved. The data suggests a description of the electronic properties of pentacene on these substrate-systems according to molecular level alignment with respect to the common vacuum level.

In contrast, pentacene on KCl/Cu(110) exhibits an energy difference between both states, that is significantly lower than the one of the lowest NIP-PIR gap of 3.1 eV of pentacene observed on a monolayer NaCl/Cu(111) [22]. Furthermore, the fact that both resonances represent the same molecular orbital of pentacene on KCl-Type /Cu(110) is a hint that a common vacuum level alignment is not applicable in this case, thus significant molecule-substrate interactions are present.

5 STM-induced luminescence from individual pentacene nanocrystals

Pentacene is a promising candidate for use in organic and optoelectronic devices. The electronic properties and structures of the organic semiconductor have been extensively studied for thin films and macroscopic crystals. Here, we report the first electroluminescence measurements from single pentacene nanocrystals using the tip of a scanning tunneling microscope (STM) as a local electrode. For localized charge injection by the STM tip, strongly red-shifted luminescence at the bulk exciton energies are observed. The emission from delocalized excitations and missing features from individual molecules reflects significant inter-molecular coupling. Excitation and emission mechanism are discussed based on the observed dependence on electrical and structural parameters.

5.1 Introduction

Organic semiconductors have made a strong entrance in nanoscale electronics and optoelectronics during the last decade. Pentacene has become the prime model system to explore the physical principles and the technological challenges associated with organic devices [16]. The extended conjugation and a favorable crystal structure are responsible for its success as organic semiconductor. On the single molecule level pentacene has also become the gold standard of local scanning probe imaging and spectroscopy. Impressive results through the use of STM [22, 23] and atomic force microscopy (AFM) [24] demonstrate sub-molecular imaging capabilities on individual molecules. Making the step from the isolated molecule to a small isolated molecular solid opens up a way to address interactions between identical molecules. Molecular crystals are bound together by weak Van-der-Waals forces and can also preserve to a large extent properties of their molecular building blocks. They can be described in a first approximation by an "oriented gas" model [96]. Essential for this study, however, is the fact that crystalline pentacene exhibits an intermolecular coupling which is comparatively strong for this class of materials. The resulting electronic dispersion becomes

largest along the direction of overlap between π-orbitals of neighboring molecules [97,18,98,99]. Pentacene is thus a material well-suited to explore consequences of inter-molecular coupling on the optical emission from the low energy electronic excitations.

Here we employ scanning tunneling microscopy and spectroscopy at 4.2 K to study charge carrier excitation and electroluminescence of individual pentacene molecules and nanocrystals with a submolecular resolution. We report on the first STM-induced luminescence from an acene. The method allows the local characterization of molecular structure, orientation, and the identification of the excited species according to their optical spectra. In combination with electronic spectroscopy and measurements of the electrical parameters for luminescence it can provide a detailed scheme of excitation and emission processes [30]. The STM tip injects charges locally into the molecular top layer. This suggests that luminescence may predominantly be emitted by a single molecule situated below the tip. This has, in fact, been confirmed in earlier studies of STM-induced luminescence on organic solids [29,28,54,32]. In the present study, in contrast, the emission line is strongly red-shifted with respect to the emission of matrix-embedded single pentacene molecules. This indicates strong inter-molecular coupling and emission from a delocalized excitation. As a result, the observed luminescence spectrum is very robust and becomes independent of the point of charge injection. The pentacene nanocrystal acts already as a molecular crystal, coupled to its top and bottom electrodes through tunnel junctions instead of Schottky contacts. It represents a bulk-like light source at the limit of small dimensions.

5.2 Growth and structure of the nanocrystals

Molecular samples were prepared and studied in ultra high vacuum (UHV). As substrates we used Au(111), Ag(111) and Cu(111) single crystal surfaces, covered by 1-2 ML of KCl. As STM tips we employed gold and silver tips prepared as described in section 3.1.2.

Pentacene nanocrystals were grown on top of these substrates in a two-step process. First, highly purified pentacene was thermally evaporated on the sample held at low temperature $T < 90$ K. The evaporation rate was low to yield a coverage of about 1 monolayer (ML) during 5 minutes evaporation time. The result is a dispersed arrangement of pentacene molecules adsorbed flat on the KCl layer. Subsequently, the substrate was annealed to 220 K for 1 minute and transferred into the STM operated at 4.2 K. The annealing step leads to pentacene dewetting on the KCl layer and to the formation of molecularly ordered

3-dimensional pentacene crystallites with tens of nm lateral dimension and a few nm height. No pentacene remains in-between the nanocrystals.

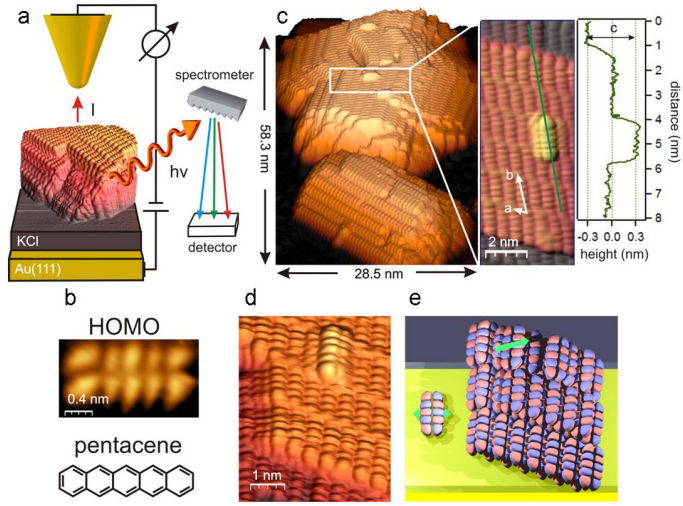

Figure 5.1. Experiment and pentacene nanocrystal structure. (a) Principle of the experiment: The tip of an STM is positioned above a pentacene nanocrystal (colored black – yellow) for imaging and tunneling spectroscopy. A tunnel current is injected into the nanocrystal decoupled from the Au(111) substrate by an ultrathin KCl layer. The emitted luminescence light is detected by an optical spectrometer. (b) Chemical structure (below) of pentacene and its HOMO orbital (above) imaged by STM for a molecule adsorbed on the KCl layer on Au(111) (U = -2.4 V, I = 10 pA). (c) STM topographic image in 3D presentation of a pentacene nanocrystal on KCl/Cu(111) and detail (right) in top view. The in-plane lattice vectors a and b are drawn in the topograph. The layer height is indicated in the height profile (green line). (d) Detail of the nanocrystal with two visible layers and an ad-molecule. (e) Model of a structure similar to (d) using a cartoon-like presentation of the HOMO orbitals with different signs of the electronic wavefunction indicated in blue and red. On the left: Top view of a flat-lying single molecule. The green arrows indicate the orientation of the transition-dipole vector for an excitation derived from transitions between LUMO and HOMO orbital. The measurements are presented using the WSxM software [75].

We find that the molecular nanocrystals nucleate at step edges, which are either due to a step in the KCl layer or a step of the metal substrate covered in a carpet-like fashion by the KCl layer. Individual pentacene nanocrystals, 3 - 15 layers thick, with lateral dimensions of a few

10 nm have been grown on top of an ultra-thin KCl layer on a metal substrate. When not stated otherwise in this chapter, the substrate is a single crystal Au(111) surface. The KCl layer acts as a tunnel barrier with a high dielectric constant providing only a small voltage drop in the external electric field of the tunnel junction. The vacuum gap between STM tip and crystal surface defines a second (tunable) tunnel barrier. In this geometry (Fig. 5.1 a) we obtained sub-molecular resolution of pentacene molecules on top of the crystal and in some cases also at the steep sides of the crystals. The nanocrystals exhibit a high molecular order with translational symmetry in which structural defects are sometimes found. The topography at the nanocrystal surface and the measured crystal heights allow us to determine the nanocrystal structure (Fig. 5.1 c,d). The lattice parameters with respect to the surface are listed in Table 5.1:

Table 5.1. Structure parameters of the pentacene nanocrystal. Note that the value c corresponds to twice the measured layer height as successive layers have different molecular orientations.

lattice vector lengths	a =	0.63 nm ± 0.03 nm
	b =	1.58 nm ± 0.04 nm
	c =	0.62 nm ± 0.1 nm
angles	angle (a,b) =	69 ° ± 3 °
	angle (long mol.axis,b) =	4 ° ± 2 °

At negative bias voltage the surface molecules are imaged through their highest occupied molecular orbital (HOMO), identified by its 5 nodes of the electronic wave function parallel to the intermediate molecular axis (Fig. 5.1 d). For comparison we show the STM topograph of the HOMO orbital of an isolated pentacene molecule adsorbed flat on the KCl layer (Fig. 5.1 b). The pentacene molecules in the nanocrystal layers are orientated with their long axis parallel to the surface and the molecular plane rotated by approximately 26° with respect to the surface plane. This rotation is evidenced by the fact that the node of the HOMO orbital along the long axis of the molecule is not seen on the closed layer but only for admolecules and step edges (Fig. 5.1 c,d). The cartoon in Fig. 5.1 e, which models a structure similar to the one shown in Fig. 5.1 d, illustrates that the rotation leads to a short a-vector between neighbouring molecules and hides the longitudinal node of the orbital from observation by the STM tip. We remark that the imaging STM tip is separated from the molecular top layer through a vacuum tunnel gap of the order of 0.5 nm - 1 nm and thus only the lobes of the electronic wave function extending into the vacuum become observable. Within experimental accuracy (see Fig. 5.1 e) the nanocrystals realize the pentacene bulk lattice structure [100]. The

strong local variations do, however, not allow to distinguish between two distinct lattices obtained by growth from solution or growth by vapor deposition [101]. The nanocrystal is markedly different from known structures of thin films on insulators on which layers are formed by molecules standing upright [97, 102].

5.3 Electroluminescence from pentacene nanocrystals

STM-induced luminescence spectra are plotted in Fig. 5.2. The upper row presents luminescence spectra recorded with the STM tip positioned on a pentacene nanocrystal for different tip materials and close-packed single crystal surfaces of different metals. The dominating peak in these spectra is situated at 1.6 eV. Spectra recorded next to these nanocrystals with the STM tip positioned above the ultra-thin KCl insulator layer are shown for comparison in the lower row. The features in these spectra are due to tip-induced plasmons localized between metallic tip and metallic substrate and depend on tip shape and tip and substrate material [41]. We emphasize that the two corresponding spectra in each column exhibit no similar features. Moreover, we find that the nanocrystal spectra in the upper row are well reproduced and the peak positions do not depend on the underlying plasmonic spectrum. We conclude that STM-induced luminescence allows to access optical spectra originating from the pentacene nanocrystals. Comparing the three typical spectra in the upper row of Fig. 5.2 to pentacene luminescence spectra in the literature we find agreement only with photoluminescence spectra from macroscopic single crystals measured at 8K [103]. There is no match to the lowest singlet transition of individual pentacene molecules which is situated at 2.30 eV for the isolated molecule [104, 105], red-shifted by dielectric screening to 2.03 eV when embedded in p-terphenyl [106] and to 1.98 eV for embedding in tetracene [107]. Pentacene electroluminescence spectra recorded from organic field effect transistor devices exhibit typically broad spectral features extending to energies above 2 eV [20]. The low temperature in our study provides sharp features, and the geometry of charge transport along the shortest crystal dimension suppresses the influence of domain boundaries with respect to thin film geometries. Optically induced luminescence from organic crystals probes bulk properties, with surface contributions being negligible.

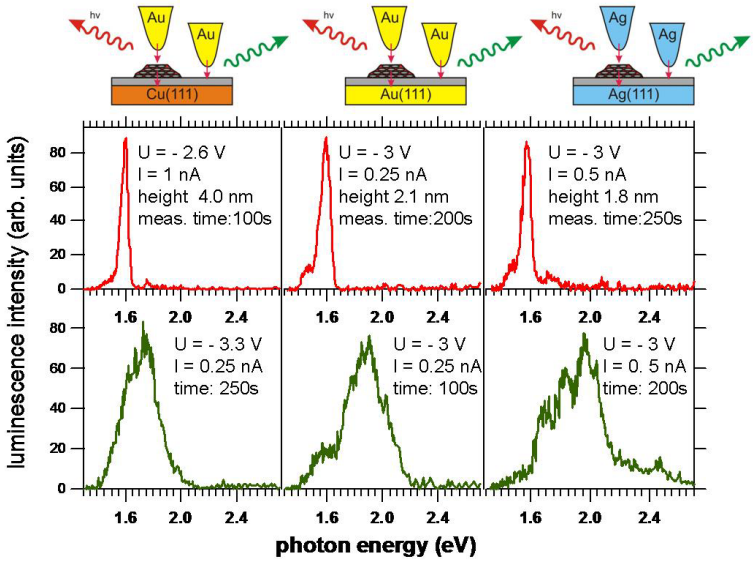

Figure 5.2. STM-induced electroluminescence. Top: Schematic drawing of the experiments shown in the color-coded spectra below. Upper row of spectra: STM-induced luminescence recorded for the STM tip positioned on the pentacene nanocrystals with the listed crystal height, spectral measuring time and tunneling parameters: bias voltage (U) and current (I). Lower row of spectra: STM-induced luminescence due to tip-induced plasmons recorded with the STM tip positioned on the KCl-covered single crystal surface.

In contrast, nanocrystals provide a high surface-to-volume ratio. The agreement of our data with single crystal photoluminescence is thus surprisingly good. It concerns peak energy, peak width, peak asymmetries and the relative peak heights. Apart from the strong peak at 1.59 eV, a shoulder around 1.45 eV is found. In addition, a small peak at 1.76 eV can be identified, which only sometimes exceeds the noise level in our spectra. Following the discussions in [103,108], we can assign the observed features to the free singlet exciton (1.78 eV), the self-trapped exciton (1.64 eV), and an impurity related line (ca. 1.4-1.5 eV). The dominance of the 1.6 eV peak can be regarded as characteristic for crystals in contrast to the 1.8 eV peak dominating for pentacene clusters and thin films [109]. Pentacene-related luminescence could only be observed at negative bias voltage and for crystallites of a minimum thickness of 1.5 nm. As the reduced dimensions of the crystallites suggest a spatial exciton confinement, we analyzed the peak position of the 1.6 eV line with respect to crystal

width and height. A shift of the peak energy could, however, not be identified within experimental accuracy and is estimated to be smaller than ca. 10 meV over the range of 1.5 nm - 4.0 nm crystal thickness. While a theoretical estimate on the confinement is not available, the assignment to a self-trapped Frenkel exciton may rationalize the small effect.

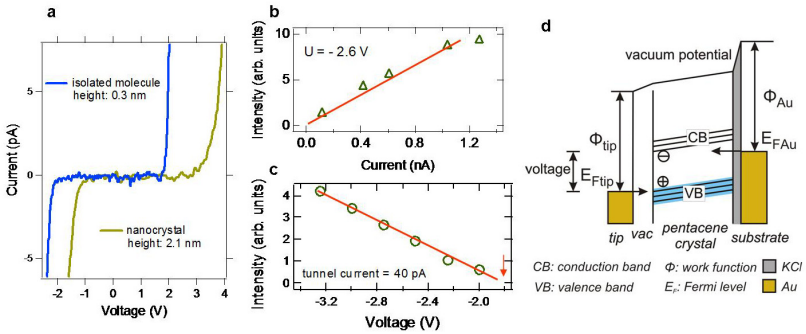

Figure 5.3. Electronic properties. (a) Tunnel current as a function of bias voltage (Au(111) substrate with respect to STM Au tip) measured on an isolated molecule (blue) and on a nanocrystal (yellow). (b) Integrated STM-luminescence intensity from a nanocrystal as a function of tunnel current for constant bias voltage. (c) Integrated STM-induced luminescence as a function of bias voltage for constant tunnel current. The luminescence collection time per point in b and c is 250 s. (d) Schematic electronic level diagram for the charge-injection geometry employed for the measurements with the bias voltage near the luminescence onset: Vacuum potential (top line), electronic levels of the metals and pentacene band structure. The two tunnel barriers are symbolized by the gray (KCl layer) and the white (vacuum) gap.

A closer inspection of the features in the STM-induced luminescence spectra finds consistent red-shifts of approximately 40 meV with respect to a 8 K photoluminescence spectrum [103]. We find that a significant part of the shift is related to the electric field between tip and sample which is of the order 1 V/nm. The shift of the peak energy of the strongest spectral feature between –3 V and –2 V bias voltage reaches almost 10 meV. This shift is remarkable and challenges the assignment of the feature to a pure Frenkel type exciton. A detailed discussion of the Stark shift will be presented in detail in Chapter 6.

The dependence of luminescence intensity of the 1.6 eV peak on the electric parameters is plotted in Fig. 5.3 b, c. The emission is linear in tunnel current and shows an onset near 1.8 V

bias voltage. The small energetic difference between onset and main emission line indicates only small losses before exciton formation. An onset even below the bulk transport threshold of pentacene (2.2 eV [110]) suggests the creation of excitons close to the position of charge injection. Electron tunneling spectra measured on single pentacene molecules on the KCl layer (Fig. 5.3 a) yield charge injection potentials of -2.4 eV for the HOMO and +2.0 eV for the lowest unoccupied molecular orbital (LUMO). The current between the HOMO and LUMO onsets vanishes already for pentacene in the first layer on the KCl buffer. This demonstrates the decoupling of the electronic states of metal and molecule. Independent of this decoupling, the HOMO and LUMO levels shift only weakly with bias voltage and changing tip-molecule separation [22], as the KCL layer is thin and exhibits a high dielectric constant. The nanocrystal tunnel spectra (Fig. 3.3 a) are offset with respect to single molecule spectra by about 1 eV to more positive voltages. This shift cannot be due to the STM-related electric field inside the pentacene because the shift is towards higher energies also at negative bias. We attribute the offset to band formation in the crystal and a reduction of work function.

Based on the presented results, we propose a scenario leading from charge injection to luminescence in the pentacene nanocrystals: The observed onset bias of luminescence at -1.8 eV (Fig. 5.3 c) suggests that, after extraction of an electron by the tip, an exciton (1.78 eV) is formed. A weak signature of its decay is observed in the luminescence. At higher bias voltage additional channels may open up. Following the assignment of transitions in the literature [103], the 1.78 eV exciton is mobile within the crystal. By self-trapping, the exciton immobilizes, losing about 0.2 eV. This exciton provides the dominant signal. Fig. 5.3 d sketches an energy diagram of the electronic levels involved in the electroluminescence near its onset. The Au electrodes inject charge carriers through their respective tunnel junctions. The electrical conductance required by STM operation is provided by the valence band. A bulk-like conduction band cannot line up with the substrate Fermi energy. Due to the low temperature in the experiment, the electrons are injected through an extended tunnel barrier, which may favor a direct exciton formation from the continuous current of holes in the valence band.

An important aspect for the understanding of the luminescence mechanism is the absence of observable molecular luminescence from isolated pentacene molecules on the insulating layer. Only for nanocrystals reaching a thickness of 1.5 nm, STM-induced intrinsic luminescence from pentacene was strong enough to become detectable. From the position of electronic states of the isolated molecule (Fig. 5.3 a) the creation of electron-hole pairs should be possible also for hole injection into the isolated molecule if we assume its HOMO-LUMO

transition at or below 2.1 eV. Two mechanisms may be responsible for the different behavior of crystal and single molecule: First, the generation of luminescence inside the nanocrystal can provide a relatively large spatial separation of the decaying exciton from the adjacent metal electrodes. Emission close to metal surfaces is known to lead to efficient non-radiative quenching e.g. due to electron-hole pair generation in the metal ([111] and refs. therein). Second, single molecules adsorb in a flat-lying geometry while pentacene molecules in the crystal are rotated around their long axis, as we showed above. The transition dipole of HOMO-LUMO-derived transitions is oriented along the intermediate molecular principal axis, as indicated by the double-headed green arrows in Fig. 5.1 e for pentacene on the substrate and in the crystal. The radiation from a flat-lying molecule is efficiently screened by the metal substrate and can in addition not couple well to tip-induced plasmonic modes which lead through tip-enhancement to a more efficient radiation into the detected far field [54, 32]. As the second mechanism, however, would not apply for the suppression of luminescence for very thin crystals, the first mechanism appears to be decisive here.

5.4 Conclusion

In conclusion, our experiments demonstrate STM-induced luminescence from an acene. Luminescence from delocalized excitons can be obtained even for highly localized injection of charge carriers from an STM tip. The interaction between neighbouring molecules provides a sufficient delocalization of the excitation to yield bulk-like emission spectra. The suppression of luminescence for ultrathin crystals suggests emission from the nanocrystal at a sufficiently large distance (>1 nm) from the metallic electrodes. The crystal structure can affect the emission conditions through the orientation of the emitting transition dipole. The experimental set-up employed in this study realizes an organic light source made of a homogeneous material with bulk-properties near its lower size limit. The results can provide a basis for studies to explore new functionalities by employing layered organic structures or single molecules embedded in host nanocrystals.

6 Stark Shift of the luminescence from pentacene

In the previous chapter we showed that pentacene nanocrystals emit bulk-like luminescence spectra. A detailed analysis of the strongest emission line in these spectra shows a continuous spectral shift with applied bias voltage in the STM which follows a Stark shift behaviour. The electric field between STM tip and its counter electrode, the substrate, can reach substantial values and can easily be increased to values three orders of magnitude larger than in typical solid state Stark shift studies, which apply fields of the order of 10 kV/cm [112,106]. Stark shifts in the electric field of an STM are well-known phenomenon and have been reported for electronic states in semiconductor quantum dots [113,114,115], surface states [116], image potential states [117], and quantum well states of metals [118].

In this chapter we measure the Stark shift to access properties of excitons in an organic material and estimate quantitatively the mixing of different exciton types. This is achieved not only through the strong electric field but also through the high energy resolution easily achieved by employing optical spectroscopy, and through the characterization of the local molecular arrangement by STM-topography with sub-molecular resolution. We report a Stark shift with the electric field vector perpendicular to the long molecular axis of pentacene which is larger than observed in earlier Stark-shift studies on pentacene molecules and films even in the direction parallel to the long axis of pentacene. The long molecular axis of acenes is the direction of their highest polarizability for singly occupied orbitals. We assign the result to a mixing of the optically active Frenkel exciton with a charge transfer exciton which provides the static dipole moment required to model the data. The electric field in the experiment can be determined from the known dimensions and properties of materials in the tunnel gap and quantitative result can be derived which may even be refined when more detailed theoretical results for pentacene become available. The study allows thus to investigate bulk properties of an organic solid at extremely high fields employing STM-induced electroluminescence in which electric field and excitation are localized on a dimension of the order of the lateral extension of the nanocrystals of tens of nanometers. The observed bulk like emission spectra suggest that the luminescence originates inside the organic crystal. We can specifically

exclude its origin at defect states near the interface to the substrate because no molecule-related luminescence is obtained for crystals thinner than 1.5 nm.

6.1 Results

The Stark shift of an electronic transition is determined by the dipole and polarizability difference between an excited state and the ground state. This study focuses on the decay of the lowest singlet exciton in pentacene. The STM is operated to generate electroluminescence below its tip at potential differences of 2 V to 4 V over a distance of 0.5 nm - 3 nm. In contrast to classical Stark shift measurements, the field inside the semiconductor depends in a more complicated way on the applied voltage, as will be discussed below. The range of applicable bias voltages is limited on the high end by the onset of electron field emission and on the low end by the fact that the energy of each charge carriers must be larger than the energy of the detectable photon. The preparation of the pentacene crystal on a single crystal metal surface covered by an ultrathin KCl layer has been described in the previous chapter.

Figure 6.1 shows a typical STM-induced spectrum recorded by charge injection at negative bias voltage into a pentacene nanocrystal. The spectrum is dominated by a luminescence line at 1.59 eV which we assigned to the self-trapped singlet exciton in a pentacene crystal. The luminescence is obtained only at negative bias voltage with an onset at –1.8 V and only for crystals heights of 1.5 nm or more (s. Chapter 5). The arrows in Fig. 6.1 mark the known transitions energies of the lowest pentacene singlet states for isolated molecules [104] at 2.31 eV, single molecules embedded in host crystals [107,119] between 2.09 eV and 1.98 eV and finally three transitions observed for macroscopic single crystals [103]. The latter correspond to the lines observed in the pentacene nanocrystals. In the following, we will focus on the transition at 1.59 eV which is red-shifted with respect to literature data on the line assigned to the self-trapped exciton. The peak energy is obtained by fitting the line with two Gaussians. While the Gaussian at lower energy models a weak shoulder, the Gaussian at higher energy represents the main peak (see the inset in Fig. 6.2). A decreasing absolute bias voltage at constant current results in a blue-shift of the main peak (Fig. 6.2 a). This means that lower electron energy leads to higher photon energy. The shift would be in the opposite direction if electron energy and photon emission were connected by a constant energy loss mechanism.

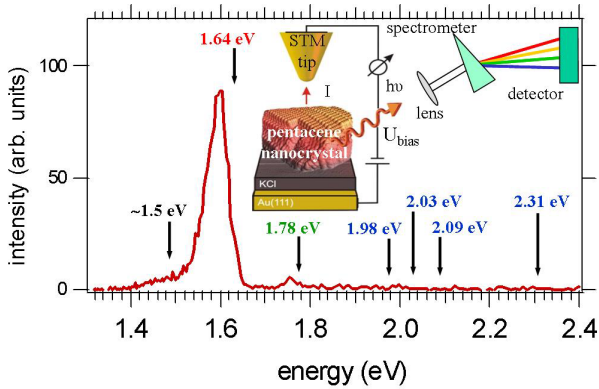

Figure 6.1. Typical STM-induced electroluminescence spectrum of a pentacene nanocrystal with the strongest transition at 1.59 eV. The arrows indicate lowest singlet transitions of pentacene in different environments, as discussed in the text. Inset: Schematic experimental set-up of STM tunnel junction and optical detection.

In STM measurements only two of the three parameters, current, voltage, and tunnel gap size, are independent. As a result, the reduction of the bias at constant current leads to a reduction of the tunnel gap. From the three parameters which can be kept constant the most stable experimental situation has been obtained for a constant current. Varying, in contrast, bias and current at constant distance leads to a drastic breakdown of luminescence at low bias and to a drastic current increase which can destroy the structure of the crystal or modify the tip at high bias. It is obvious that even minor modification of the tip during such a ramp will provide inconsistent data. The whole series in Fig. 6.2 a was accomplished within approximately 30 minutes. The good reproducibility of the data is demonstrated by the three data points at -3.0 V bias which were measured repeatedly in the series. Finally, the change of tunnel gap as a function of voltage was recorded (Fig. 6.2 b).

In order to determine the Stark shift in units which allow a comparison to literature data and calculations, the applied bias voltage has to be transformed into the electric field strength inside the pentacene crystal. Fig. 6.3 shows a schematic diagram of the energy levels as a function of the spatial coordinate from STM tip to metallic substrate. The electric field inside the pentacene crystal corresponds to the slope of the vacuum level (uppermost line) across the pentacene crystal thickness d.

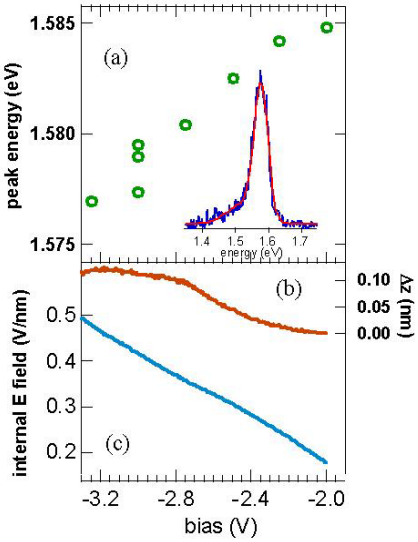

Figure 6.2. Peak energy (a) of the strongest observed transition (Fig. 6.1) as a function of bias voltage in the STM. Inset: A fit with two Gaussians (red line) is employed to determine the peak maximum. (b) measured change of the vertical tip position, i.e. tunnel gap width with bias. (c) Electric field in the pentacene crystal calculated using eq. (6.1) and the parameters discussed in the text.

Using the model for a plate capacitor made of different plate materials and partially filled with a dielectric, we obtain for the electric field inside the pentacene crystal

$$E_{pentacene} = \frac{U_{bias} + \phi_{substr} - \phi_{tip} - \Delta\phi_{KCl}}{\varepsilon\,(z + \Delta z) + d} \qquad (6.1)$$

in which $\phi_{substr} - \phi_{tip} = 0.2$ eV represents the work function difference between a closed-packed substrate surface (here gold) and the rough, polycrystalline STM tip of the same material [92]. $\Delta\phi_{KCl} = 1.6$ eV is the work function change due to the ultrathin KCl layer (s. section 4.3) which serves as an insulator between the metal single crystal and the pentacene nanocrystal.

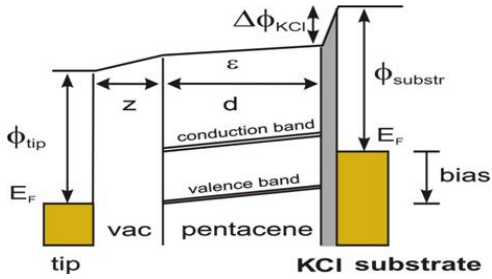

Figure 6.3. Schematic diagram of energies between STM tip and single crystal substrate. The symbols and their values are discussed in the text.

The vacuum potential difference between tip and sample is thus 1.4 V smaller than the applied bias voltage. The crystal thickness d = 2.3 nm is obtained from topographic STM scans of the crystal, and the dielectric constant of pentacene ε = 2.8 is taken from [120] for an electric field direction perpendicular to the long molecular axis (c-axis). The known change of tunnel gap Δz in Fig. 6.2 b is added to the assumed minimum tunnelling gap of z = 0.5 nm in the measurement. The absolute value z cannot be measured precisely in experiment and thus represents the largest uncertainty in (6.1). Only values between 0.2 nm (atomic contact) and 1 nm appear, however, physically reasonable for the experiment. The uncertainty of z leads to a systematic error of the calculated electric field of 25 %. Fig. 6.2 c plots the electric field as a function of bias calculated with (6.1) using the discussed parameters. In Fig. 6.4 we plot the luminescence energy as a function of the calculated field for the data in Fig. 6.2 (blue) and for a second data set measured on a pentacene nanocrystal on a KCl-covered Ag(111) single crystal surface (green).

Parabolic fits to the data provide the parameters listed in Table 6.1. From the two coefficients B we obtain the polarization difference between the radiating excitonic state and the ground state $\Delta\alpha = 900$ Å^3. The systematic error of this value is 50 %. As the electric field is oriented perpendicular to the metallic substrate surface and the long axis of the pentacene molecule is oriented parallel to the surface we measure the Stark shift of the singlet exciton decay at 1.6 eV in the direction perpendicular to the long molecular axis.

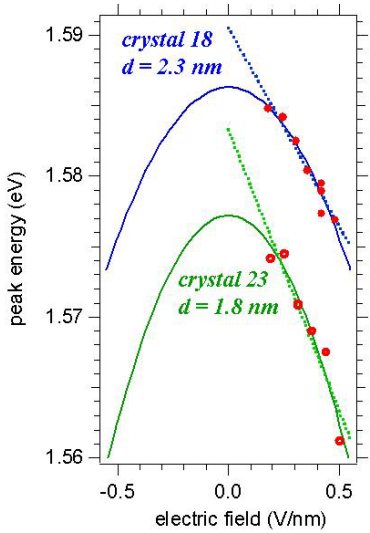

Figure 6.4. Experimental peak positions (red markers) plotted as a function of the calculated electric field inside pentacene for a 2.3 nm high pentacene nanocrystal on Au(111) (filled circles) and a 1.8 nm high nanocrystal on Ag(111) (open circles). The solid and dotted curves are parabolic and linear fits, respectively, to the data sets.

Table 6.1. Parameters for the best fit curves in Figure 6.4. The symbol *e* in the units of parameter A is the elementary charge.

Pc crystal		**line fit** $U(E) = U_0 - A \cdot E$			**parabola fit** $U(E) = U_0 - B \cdot E^2$		
no.	height	U_0 (*eV*)	A ($e \cdot nm$)	$\Sigma \chi^2$	U_0 (*eV*)	B ($eV/(V/nm)^2$)	$\Sigma \chi^2$
18	2.3 nm	1.591	0.028	0.38e-05	1.586	0.043	0.34e-05
23	1.8 nm	1.583	0.040	1.19e-05	1.577	0.059	0.63e-05

6.2 Comparison to the literature.

Experimental data in the literature suggest polarizability changes of the lowest singlet transition in pentacene of approximately $\Delta\alpha$ = 200 Å^3 [121,106]. None of the earlier studies, however, investigate exactly the property which we measure: ref. [121] measures the angular average in crystallites on the 1.834 eV transition, i.e. the free exciton at an energy 0.2 eV

higher than the transition we measure. The other experiment [106] investigates single molecules in p-terphenyl with the electric field along the long molecular axis. A third, deviating experimental study [112] is not discussed here since it has already been critically commented by its authors. There is no calculation of $\Delta\alpha$ available for pentacene. In the following, we use a calculation of pentacene polarizabilities in different charge states [120] to obtain a coarse estimate of $\Delta\alpha$: The singly charged cation and anion of pentacene have a much larger polarizability than the neutral ground state. This applies, however, predominantly for the polarizabilities along the long molecular axis, LL. The two other diagonal elements corresponding to the intermediate axis (MM) and the molecular normal (NN) do not change significantly with charge state. If we approximate the excitonic polarizability change as the polarizability of the cation plus the polarizability of the anion minus twice the polarizability of the molecule in the ground state, we obtain for the principle axes: $\Delta\alpha_{LL} \approx 70$ Å^3, $\Delta\alpha_{MM} \approx 1$ Å^3, and $\Delta\alpha_{NN} < 1$ Å^3. For comparison, a full calculation of $\Delta\alpha$ for tetracene, the next smaller acene with comparable properties, yields $\Delta\alpha_{LL} = 173$ Å^3 and $\Delta\alpha_{MM} = -3$ Å^3 [122]. As we can exclude the observation of the $\Delta\alpha_{LL}$ component from the topographic study of the sample, we conclude that our data cannot be accounted for neither by the experimental observation nor by theory. Both of the discussed theoretical sets of $\Delta\alpha$ apply, however, to single molecules without taking into account the surrounding solid. The molecular environment induces non-local effects which have been discussed for polyacenes already since the 1980s [123,124]. Recent sophisticated calculations have modelled the mixing of Frenkel and charge transfer (CT) excitons for perylene-based pigments [125]. An experimental study of pentacene by electron energy loss spectroscopy (EELS) finds a deviation of the singlet transition from a pure Frenkel state [126]. The calculation of the lowest excitons in pentacene by Tiago *et al.* identify a strong charge transfer character of the lowest singlet exciton situated at 1.6 eV/1.7 eV [101]. While this appears to be in excellent agreement with our data, a detailed comparison is not possible as both the static dipoles and transition dipole strengths of this transition are not available. The observation of a pure CT state in our study appears unlikely as these states decay with a strongly reduced oscillator strength [96]. If we construct in a simplified model a static dipole of a CT exciton by elementary charges on nearest neighbors (at the vertical layer distance of 3 Å) we obtain a value of 3 eÅ (see Fig. 6.5). Then a CT contribution of about 10 % to the Frenkel exciton would be consistent with the observed dipole. A constant mixing ratio will, however, yield a linear Stark effect because the CT-dipole is not induced but only oriented by the electric field. Testing a linear dependence on the data, we find (Fig. 6.4) that the fit is only little worse (s. Table 6.1) than the parabolic fit

when judged by the sum of squared errors $\Sigma \chi^2$. We remark that the comparison between linear and parabolic fit are valid as both have exactly two free parameters. The fact that luminescence is not observable at or below its onset voltage around 1.8 eV reduces the sensitivity of the measured data sets to discriminate between a linear and a quadratic Stark shift. We want to point out that the mixing of Frenkel and CT exciton might be increased by the strong electric field. This field is, however, not strong enough to overcome the binding of electron and hole in the excited state. Based on our observation that the luminescence intensity increases monotonically with increasing absolute bias (at constant current) our data do not indicate an exciton ionization (or dissociation) up to electric fields of 0.5 V/nm.

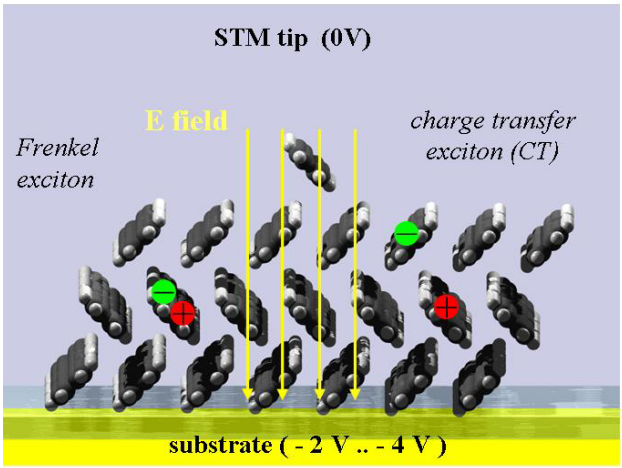

Figure 6.5. Perspective view (with slightly elevated viewpoint) of the molecular arrangement of pentacene inside a nanocrystal adsorbed on KCl/closed-packed single crystal surface. The electric field direction at negative bias is indicated by the yellow arrows. On the left hand side the separated charges of an excited state localized on a single molecule (Frenkel exciton) is drawn. The right hand side illustrates a charge transfer exciton with charges located on neighboring molecules.

6.3 Conclusion

In conclusion, a Stark shift is observed for the lowest singlet transition of pentacene nanocrystals in STM-induced electroluminescence. From the nanocrystal structure we conclude that the electric field is applied in the direction perpendicular to the long molecular axis of the pentacene molecules. Despite a systematic error coming from the calculation of the electric field inside the pentacene crystal, the observed polarizability change in the transition is clearly larger than expected from earlier experiments and calculations. This suggests a mixing of Frenkel and CT exciton. A more detailed understanding of the observed Stark shift would require a sophisticated model also taking into account the strength of the applied electric field.

7 Photon correlation measurements on STM - induced luminescence

The study on STM induced luminescence discussed in the earlier chapters is focused on the spectral properties of the emission. Optical spectroscopy is a means to distinguish the intrinsic molecular luminescence from the plasmonic "background" emission and to clarify the excitation mechanism. However, the light spectra give no information on the excitation dynamics and the spatial localization of the emission. Especially if electroluminescence from molecular aggregates is studied, the question arises if the light is emitted by only one particular molecule incorporated in the structure. The tunnel current of the STM tip used for excitation is highly localized since STM topography reaches sub-molecular spatial resolution. This suggests that tunneling over a molecule incorporated in the top layer of the structure leads also to a localization of the excitation on this particular molecule. In order to unambiguously clarify if the light source is a single molecule, the statistics of the time delays between the photons has to be investigated. The observation of antibunching in the photon statistics of emitted light can prove the existence of a single photon source like an individual molecule. Anti-bunching has not yet been demonstrated experimentally for STM-induced luminescence. For such studies, a set-up for photon-correlation measurements in the STM was built and taken into operation during the work on the thesis.

7.1 The Hanburry Brown and Twiss interferometry

In the 1950's Hanburry Brown and Twiss developed a technique for measuring the correlation of light intensity fluctuations. The principle was demonstrated in a laboratory experiment with a mercury discharge lamp as a light source [127]. The arrangement is shown in Fig. 7.1 and will be referred to as a HBT experiment in the following. The filtered 435.8 nm line from the lamp is split by a half-silvered mirror and fed into two photomultipliers PMT1 and PMT2.

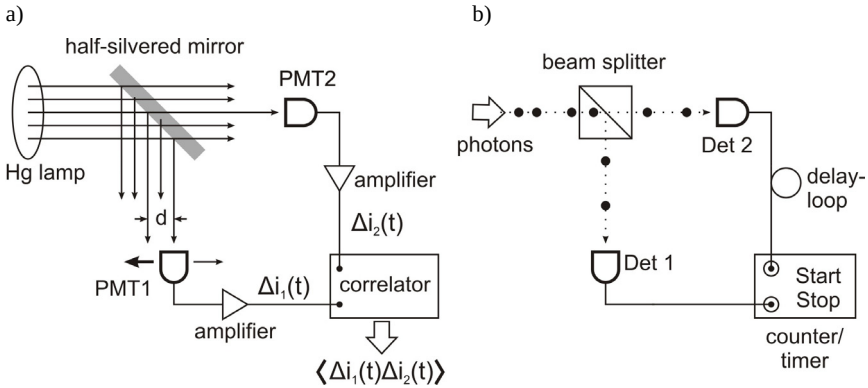

Figure 7.1. (a) Original set-up for the measurement of intensity correlations [127]. (b) Modified HBT configuration for the measurement of photon correlations (after [128]).

The photocurrents i_1 and i_2 generated by the detectors are amplified by an AC-coupled amplifier and the output signals are proportional to the fluctuations Δi_1 and Δi_2 of these photocurrents. PMT1 is mounted on a stage movable in the direction normal to the beam. In this way PMT1 can detect intensity from different points of the source in contrast to PMT2, which is fixed. The two signals are connected to a correlator, by which they are multiplied and averaged over time. Finally, the output signal is proportional to $\langle \Delta i_1(t)\Delta i_2(t)\rangle$. Since the photocurrents i_1, i_2 are generated by the incident light intensities ΔI_1, ΔI_2, the signal is also proportional to $\langle \Delta I_1(t)\Delta I_2(t)\rangle$. The brackets denote the time averaging. The outcome of the experiment can be fully explained by classical properties of light and gives a measure for its coherence. If the distance d is increased (s. Fig. 7.1 a), the spatial coherence of the light detected by both detectors decreases, i.e. the output signal decreases. Since for $d > 0$ different points of the light source are being probed, the corresponding signals ΔI_1 and ΔI_2 are no more correlated and for large d the output tends to 0. The original HBT experiment was used for the measurement of star diameters. The spatial coherence of stellar light as a function of distance d between the photomultipliers is a measure for the angular spread of the star's light. From the angular spread of the emission, the stellar diameter can be deduced, assuming that the distance to the star is known.

After a slight modification, the HBT experiment can further access the quantum properties of the analyzed light [128]. Instead of photomultipliers, single-photon counting detectors can be used, connected to the start and stop inputs of an electronic counter (timer). One of the

outputs is delayed by a time τ_D through the use of a longer cable for the connection, which causes the output pulse signal of one of the detectors to travel a longer distance to the counter. This is necessary in order to record shorter time intervals compared to the dead time of the counter and the detectors. The main consequence of the modification is that single photons are collected rather than total light intensity integrated over a certain time period. Upon a photon impingement at the first detector, an electronic pulse is generated, which starts a clock. The clock is stopped by a pulse generated by the second detector upon photon arrival and the elapsed time between both events is recorded. In contrast to the original HBT experiment from 1956, the photon number fluctuations are measured as a function of time and not as a function of the spatial position of the detector. Typically, the result is represented as a histogram of the number of recorded start-stop pairs for each particular time period. For a quantitative description of the experiment's outcome, the second order correlation function $g^{(2)}(\tau)$ is used:

$$g^{(2)}(\tau) = \frac{\langle n_1(t) n_2(t+\tau) \rangle}{\langle n_1(t) \rangle \langle n_2(t+\tau) \rangle}, \tag{7.1}$$

where $n_{1,2}(t)$ is the number of detected photons on each detector at time t. It is a measure for the simultaneous probability for a photon-detection at time t by detector 1 and a photon-detection at time $t+\tau$ by the detector 2. Finally, $g^{(2)}(\tau)$ is proportional to the probability to detect a photon at time $t = \tau$ after a photon was detected at time t=0. The same probability is represented by the time histogram of the HBT experiment, which is a direct measure of the second order correlation function. The value of $g^{(2)}$ differs from the time histogram, because of its normalization, which is obtained by assuming that $g^{(2)}(\tau)$=1 for very long time delays.
The photon statistics exhibits a characteristic signature depending on the light source. There are generally three classes of light sources, distinguished by the form of $g^{(2)}(\tau)$ around $\tau = 0$ (s. Fig. 7.2).

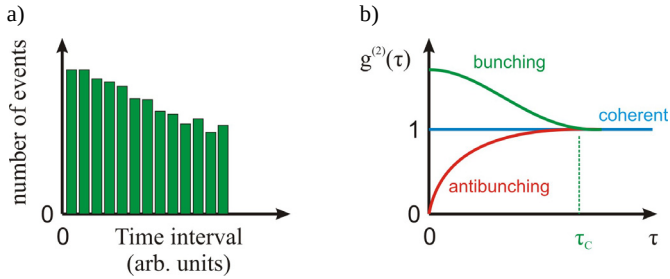

Figure 7.2. (a) Schematic time histogram of recorded start-stop events of incident photons. (b) Schematic form of the second order correlation function for the three characteristic types of light sources.

Perfect laser light shows no intensity fluctuations, i.e. the distribution of time delays between the photons is random. This results in a constant value of $g^{(2)}(\tau)=1$. In contrast, the phase of the different emitting atoms in a thermal source fluctuates. This type of light sources tends to emit photons in bunches. This gives rise to the larger value of $g^{(2)}(0)>1$, which decreases within the so-called coherence time τ_C, characteristic of the microscopic emission process.
An exponential fit to the time-histogram of photon-pair counts in the form,

$$N = e^{-t/\tau}, \tag{7.2}$$

gives the lifetime τ of the corresponding radiative or decay process.

7.2 Antibunched light

Systems consisting of an ensemble of light emitters like the atoms in a discharge lamp, in a star, or the building blocks of the laser active medium, tend to emit photons simultaneously, which is represented by the value of $g^{(2)}(0)$, being larger or equal to 1. However, if the light source emits a train of individual photons, well separated from each other in time, the experiment has a different outcome. In this case, the second order correlation function is zero at time $t = 0$, which means that there is no probability to detect more than one photon at the same time (s. Fig. 7.2 b, green). Such properties can be explained by quantum mechanics and are characteristic of two-level systems. An individual atom or molecule undergoing an electronic transition between two discrete energy levels is not capable of emitting more than one photon at a time. After an electronic transition to the ground state has taken place, the two-level system needs time in order to be excited again, i.e. until it emits the next photon.

The separation of the photons by time delays gives rise to the so-called antibunching effect or anticorrelation in the photon statistics. It results in a value of $g^{(2)}(0) = 0$ in the ideal case. The effect appears as a dip in the time histogram of the recorded photon-pair times at time zero. It can be reduced, i.e. the $g^{(2)}(0)$ does not fall to zero, if there are additional signal contributions like stray light, dark noise of the detectors or the simultaneous emission of more than one emitter.

Antibunching was experimentally observed for the first time on an atomic beam of Na atoms by Kimble *et al.* [129]. The authors used laser excitation on an atomic beam. The collected fluorescence signal came from not more than 1 or 2 atoms on average. Later, the preparation of organic host-guest systems turned out to be a successful approach to isolate individual organic molecules and to study their emission line. Antibunching was demonstrated by laser excitation on individual pentacene molecules at low temperatures [55] and terrylene molecules at room temperatures [130], both embedded in a p-terphenyl matrix. In the above mentioned studies, the isolated organic emitters were suspended in a dielectric environment. Antibunching was also reported for Rhodamine 6G molecules immobilized on a silica surface [131] and for semiconductor quantum dots [132, 133].

A study of the photon statistics on organic molecules on a metal surface was reported by Perronet *et al.* [60]. Organic molecules suspended in solution were placed in the tunnel junction of an STM. In this first experiment employing the HBT technique in the STM, no intrinsic luminescence was generated. Light emission was due to plasmon excitation modified by the organic molecules between the metallic tip and sample. The photon correlation measurements on this plasmonic emission show photon **bunching**, which was attributed to fluctuations of the number of molecules in the tunnel junction. By now, there is no report on intrinsic STM-induced molecular luminescence showing **antibunching**.

7.3 Experimental details

During the work on the thesis, an experimental setup for time correlation measurements on the STM-induced luminescence was built and taken into operation (Fig. 7.3). Basically, it follows the configuration in Fig.7.1 b. The main difference is the separate coupling of two independent light beams originating from the STM tunnel gap into each of the detectors. By this approach a higher efficiency of light collection can be achieved in comparison to the HBT configuration, in which a single light beam is split into two parts by a beam splitter. In our set-up, the light is detected from two different directions. If a single photon emitter is the

source of light, the outcome of the experiment is identical to the one of the HBT-configuration.

Two PerkinElmer silicon avalanche photodiodes (APD) SPCM-AQRH-15 with dark count rates of 50 counts per second are used. These APD's are capable of single photon detection in the wavelength range of 400 - 1060 nm with a very high efficiency (>65% at 650 nm). The active area of the photodiodes has a diameter of 180 µm. A challenging issue is the coupling of the point-like source of light emission coming from the STM tunnel junction onto the active area of the APD's. In order to enable an *in situ* adjustment, the detectors were mounted on high-precision translational stages driven by stepper motors. The adjustment of the optical system was performed by maximizing the counting rate of plasmonic emission from the STM in tunneling contact.

For the time correlation measurements the two detectors are connected to the start and stop inputs of a time-correlated single photon counting module (Becker & Hickl SPC-130). The response of one of the detectors is delayed by a 20 m long cable, which introduces a time delay of ≈ 100 ns. In the counter, start-stop events are recorded within time bins of 216 ps. In Fig. 7.3 b, a measurement of photon-pair events on a clean Au(111) surface using a Au-tip is shown.

The two peaks of positive correlation in Fig. 7.3 b) are due to light coming from the one APD and detected by the other APD. The active light emission of the APD results from the delayed recombination of electrons and holes generated in the avalanche process. Thus, the delay time of the peak onsets reflects the time that light takes to travel from one APD to the other through the optical paths with reflection at the STM-tip. The decay of the peak corresponds to the lifetime of the hot electron-hole pairs in the APD [134]. Although at first sight, this is an unwanted feature, the effect gives the opportunity to calibrate the set-up. First, the upper limit of the time resolution is estimated to be 0.5 ns. Second, the position of the correlation time $t = 0$ on the x-axis can be exactly determined, since it is symmetric with respect to the correlation peaks. This symmetry is provided by the fact that the distances from each detector to the tunnel junction (the source of light) are equal.

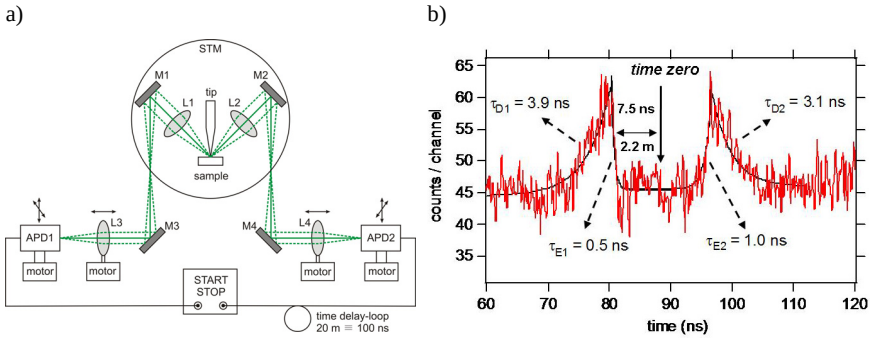

Figure 7.3. (a) Scheme of the set-up after HBT for measuring photon statistics in the STM. The light originating in the tunnel junction is coupled over two separate light paths into the APD's. (b) Histogram of photon correlation with a Au-tip on Au(111), tunneling parameters: 3V, 1nA, integration time: 2000 s. The arrow denotes the position of the time zero. The distance in time between both peaks corresponds to the optical path length from APD1 to APD2 (green solid line in (a)). By fitting the peaks according to eq. (2) the lifetime of the afterpulsing excitation $\tau_{E1,2}$ and decay $\tau_{D1,2}$ are determined.

7.4 Photon statistics of the electroluminescence from pentacene nanocrystals

First measurements of photon correlations were performed on the luminescence from pentacene nanocrystals grown on Au(111). Photon pair coincidences were recorded on light emission generated with the tip at a fixed position over the top layer of the crystal. In Fig. 7.4, the photon statistics is shown, measured on the luminescence from a pentacene crystal of 3 nm height. In the time histogram there is no dip at time $t = 0$, which can be distinguished from the noise level. As discussed in the previous chapters, the luminescence from pentacene in the STM is attributed to a recombination from the self trapped exciton. The absence of the antibunching dip is consistent with a delocalized exciton recombination.

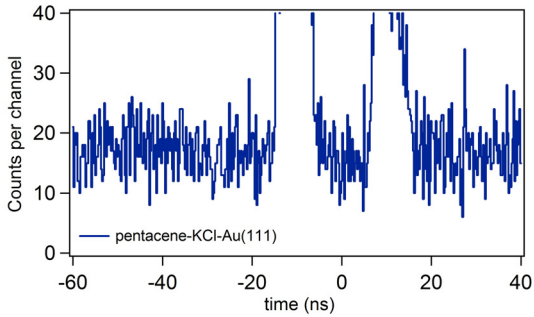

Figure 7.4. Time histogram of photon pairs measured on a pentacene nanocrystal. Tunneling parameters: -3.3 V, 1 nA. Integration time: 9.6 h. Counting rate of the APDs: ~2000 counts/s.

This is supported by the measurement shown in Fig. 7.5. We recorded a light map during a constant current topography scan over a pentacene nanocrystal. The light intensity shows no modulation related to the molecules in the top layer.

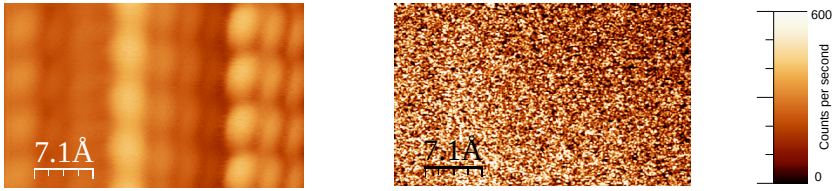

Figure 7.5. STM-topography (left) and corresponding light map with color scale (right) measured on the top-layer of a pentacene nanocrystal of 3 nm height. The light intensity image represents the amplified signal from APD1. Tunneling parameters: -3.3 V, 8 pA.

This observation demonstrates that the excitation mechanism is not sensitive to the tunneling position. Charge injection (defined by the constant current during the scan) on a molecule or between the molecules has no influence on the emission yield. This is consistent with the picture that excitons, once created, are mobile inside the crystal. Thus, multiple excitons could form and radiate simultaneously at different sites, and do not localize at the molecule below the tip. However, it should be noted that the experimental resolution of the photon statistics measurement is limited to 0.5 ns. If the lifetime of the exciton is much smaller, then anticorrelation may exist, even though it is not observable.

7.5 Comparison to C_{60} nanocrystals

We measured photon statistics on another system, which suggests a different behavior compared to pentacene. In Fig. 7.6, STM topography and corresponding light map are shown, taken on a C_{60} - nanocrystal of 3 nm height. The crystal is built out of 3 molecular monolayers of hexagonally ordered C_{60} fullerenes and was grown on KCl on Au(111).

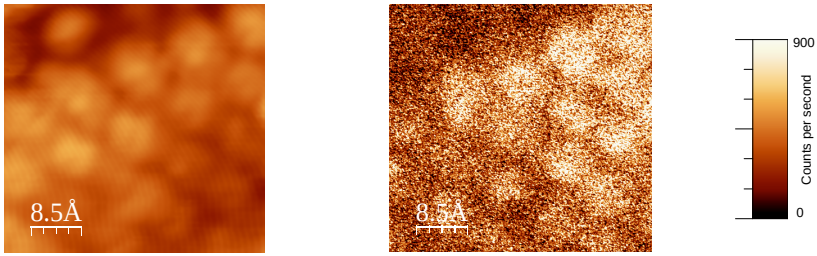

Figure 7.6. STM-topography (left) and simultaneous light map (right) from APD1 with color scale measured on the top-layer of a C_{60} nanocrystal of 3 nm height. Tunneling parameters: -3.3 V, 200 pA

In contrast to pentacene, the light emission is spatially modulated by the molecules of the top layer. STM-induced fluorescence from C_{60} has been observed on nanocrystals comprising 3 monolayers of molecules, grown on ultrathin NaCl/Au(111) [28, 32]. Structures in the light maps on C_{60} monolayer on Au(111) showing correlation to the position of the molecules was reported by Berndt *et al.* [52]. The authors suggest that the source of light emission is localized on the individual molecule below the STM-tip. This motivated us to perform time correlation measurements on this system (s. Fig. 7.7). However, the photon statistics shows no evidence of antibunching.

There are a few possible explanations for the missing anticorrelation feature. First, after charge injection into the top-layer molecule, hopping of the excess charge to neighbouring C_{60} molecules in the underlaying layers may occur. This process is fast and takes place in the time scale below 2 fs [135], being 3 orders of magnitude smaller than the excited state lifetime, which is below 500 ps [111, 136]. Excess charge hopping could thus lead to a simultaneous excitation and radiation of more than one molecule, which would, of course, strongly reduce the anticorrelation effect.

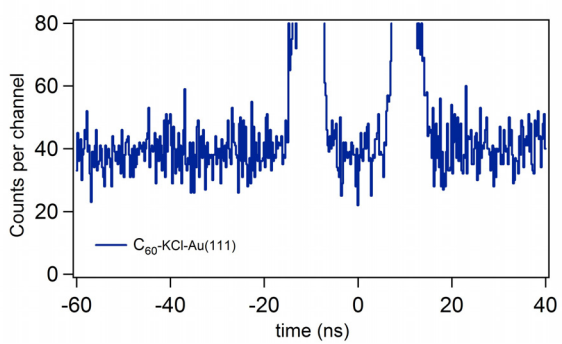

Figure 7.7. Time histogram of photon pairs measured on a C_{60} nanocrystal. The statistics shown is the sum of two independent measurements on nanocrystals of 3 nm height. First: tunneling parameters: -2.8 V, 0.5 nA, integration time: 8.6 h.; second: tunneling parameters: -3V, 0.6 nA, integration time: 3.7 h. Counting rate of the APDs: ~ 2500 counts/s.

A second explanation is related to the lifetime of the excited state compared to the time resolution of the photon-correlation set-up. It is known that near a metal surface the lifetime of the excited state of C_{60} is reduced by an order of magnitude below 0.5 ns [111], which is the time resolution of our set-up. For this reason an anticorrelation dip in photon statistics might be not visible, even if charge hopping does not take place and the light emission comes from a single molecule. Especially the vicinity of the metallic tip is a strong energy dissipation source causing fluorescence lifetime reduction. Moreover, a small plasmonic background accompanying the fluorescence could be present, which may destroy or strongly reduce the antibunching dip.

7.6 Conclusion and perspectives

When measurements of photon statistics on molecules excited by the STM are performed, two critical issues have to be considered. These are the emission yield and the lifetime of the excited state of the molecular luminescence. Both are strongly modified in the STM-tunneling junction compared to the gas phase or solid state. First, the efficiency of the process determining the number of detected photons is crucial for obtaining good statistics in the time histograms. A dip in the photon statistics indicating antibunching can only be identified if it is considerably stronger compared to the noise level of the number of start-stop events. If a single photon source is present, it will induce a minimum at time $t = 0$ with a value smaller

than 50 % of the mean number of detected events per channel. The signal-to-noise ratio of the measurements on clusters of pentacene and C_{60} presented here is already at the lower limit, at which an antibunching peak could still be identifiable.

The second important parameter, the lifetime of the radiating state, should be larger than the time resolution of the set-up. One approach for overcoming the lifetime reduction near the metal electrodes is to use molecules with intrinsically longer excited state lifetimes. Phosphorescence emitters might thus be better candidates for time-resolved electroluminescence studies in the STM. However, one should be aware that the emission yield of intrinsic luminescence represented by the efficiency η and the radiative lifetime τ_{rad} are inversely proportional:

$$\eta = \frac{k_{rad}}{k_{rad} + k_{nonrad}}, \tag{7.3}$$

where $k_{rad} \propto 1/\tau_{rad}$ and $k_{nonrad} \propto 1/\tau_{nonrad}$. The decay rates k_{rad} and k_{nonrad} of the radiative and non-radiative process are inversely proportional to the corresponding lifetimes τ_{rad} and τ_{nonrad}. This simple relation tells us that an increase in lifetime alone automatically leads to a reduction in emission yield. Thus, a suitable approach for making a molecular antibunching effect measureable in the STM implies both the increase in radiative lifetime and additionally the reduction of quenching effects, which means a reduction of k_{nonrad} (s. eq. 7.3).

8 Summary and Outlook

In this thesis, a new design for an optical access to the tunneling region of a low temperature STM has been introduced and applied. The realized set-up has three independent free propagating light channels for investigating STM-induced luminescence, giving the opportunity to efficiently collect the emitted light and to employ versatile analyses. Worth mentioning is the possibility to do optical spectroscopy and photon correlation measurements simultaneously.

The properties of pentacene molecules decoupled from metal substrates by ultrathin insulators have been investigated by STM imaging and spectroscopic measurements. The decoupling of adsorbed organic molecules does not only depend on the insulator but also on the crystal face of the metal substrate. While ultrathin layers of KCl on close-packed noble metals of Au(111) and Cu(111) provide very good electronic decoupling, pentacene on KCl/Cu(110) obtains an electronic configuration suggesting strong molecule-substrate interactions.

The KCl/metal systems with good electronic decoupling were employed as a template for the growth of pentacene nano-scale crystals. By high resolution imaging we could identify the molecular orientation in the nanocrystals and attribute their structure to the pentacene bulk phase. We observed STM-induced molecular luminescence from pentacene nanocrystals, whereas luminescence lines from individual molecules directly on the insulator could not be obtained. At crystal thicknesses where pentacene shows luminescence undisturbed by plasmonic emission, the spectra are already bulk-like, which allows the assignment to excitonic transitions. The strongest luminescence line is found to shift as a function of the applied bias, in a way that is characteristic of the Stark effect. The surprisingly large line shift with the electric field in the pentacene crystal indicates a large change of the dipole when the exciton decays. This suggests a mixing of the Frenkel type exciton with a few percent of charge-transfer character.

Finally, we implemented a set-up allowing to measure photon correlations of the STM-light emission. So far, we found no anti-correlation dips. While this is consistent with the delocalisation due to excitons for pentacene nanocrystals, the similar result for C_{60} indicates

that other parameters like, e.g. short exciton life times, can also make the anti-correlation unobservable.

Outlook

Our photon correlation measurements allow us to draw some important conclusions for future experiments. The question is: for which conditions is it possible to obtain a single photon emission from molecules in STM near conducting surfaces? To the best of our knowledge, this question has not been answered so far. As discussed in Chapter 7, the relation between radiative lifetime and non-radiative quenching of the molecular luminescence is important. Apart from the choice of molecules with an intrinsically long excited state lifetime, quenching effects due to the metal electrodes has to be minimized. For this, three different solutions can be suggested. First, a better decoupling by a thicker insulating layer may be successful. This has been tried to some degree in this thesis. However, it also strongly affects the stability of the tunneling conditions, tip geometry, and its electronic properties during an STM-scan. A solution would require to find a way of stabilizing the tip for extended times, e.g. by the use of an integrated AFM scanning mode to the STM tip which would make the long topographic scans on the insulator/organic layer more stable. A second approach to overcome lifetime reduction of the molecule due to metallic quenching is to substitute metals by semiconductors. This applies to both tip and substrate. Materials like n-doped Si or the transparent ITO would provide the conductivity needed for STM while the quenching of luminescence will be lower than for metals. A further approach is to increase decoupling of the emitter by a buffer layer of a different molecule. An extended molecular layer like C_{60} on a metal provides a larger effective distance to the substrate compared to KCl or BN, with approx. 1 nm for each C_{60}-layer. A guest molecule can be deposited in a low concentration on top of, or even sandwiched between, multiple layers of the host molecule. By tuning the height of the host system, quenching may be minimized, which leads to a higher luminescence efficiency and smaller radiative lifetime reduction. However, the excitation transfer between host and guest has to be considered. Such a diffusion of excitation can destroy any single photon emission anticorrelation, unless the luminescent transition occurs only on one guest molecule. A way to exploit this behaviour would be the doping of a crystal with guest molecules at low concentration with a red-shifted emission with respect to the host. In such systems an efficient energy transfer directed from the host to the guest system can be achieved [137]. Additionally, a guest molecule with a smaller HOMO-LUMO gap compared to the host matrix, can act as an

electron or a hole trap [138,139]. In this way, charge injection into the host system leads to an exciton forming preferentially at the guest molecule, which is implemented inside the host-system volume. The exciton recombination site would be localized at the guest molecule and should show the properties of a single photon emitter.

Organic structures providing clearly distinguishable spectral features between the host and the guest molecules would be a suitable playground for probing the localization of luminescence excitation on individual species. Finally, the unambiguous identification of a single photon source by STM-induced luminescence is still to be demonstrated. This drives the motivation to work in that field, which still bears exciting phenomena involving light generation at the nano-scale.

Bibliography

1. Andrade, B. W. D. & Forrest, S. R. White Organic Light-Emitting Devices for Solid-State Lighting. *Adv. Mater.* **16**, 1585 (2004).
2. Sun, Y. et al. Management of singlet and triplet excitons for efficient white organic light-emitting devices. *Nature* **440**, 908 (2006).
3. Reineke, S. et al. White organic light-emitting diodes with fluorescent tube efficiency. *Nature* **459**, 234 (2009).
4. Gustafsson, G. et al. Flexible light-emitting diodes made from soluble conducting polymers. *Nature* **357**, 477 (1992).
5. Guang-Feng, W. & et al. Flexible organic light-emitting diodes with a polymeric nanocomposite anode. *Nanotechnology* **19**, 145201 (2008).
6. Sony. http://www.sony.com/ces/blog/11-flex-oled.php. (2009).
7. Zhou, L. et al. All-organic active matrix flexible display. *Appl. Phys. Lett.* **88** 083502 (2006).
8. Bharathan, J. & Yang, Y. Polymer electroluminescent devices processed by inkjet printing: I. Polymer light-emitting logo. *Appl. Phys. Lett.* **72**, 2660 (1998).
9. de Gans, B. J., Duineveld, P. C. & Schubert, U. S. Inkjet Printing of Polymers: State of the Art and Future Developments. *Adv. Mater.* **16**, 203 (2004).
10. Villani, F. et al. Inkjet Printed Polymer Layer on Flexible Substrate for OLED Applications. *J. of Phys. Chem. C* **113**, 13398 (2009).
11. Gerhard, H. & Friedrich, J. Poly(alkylenedioxythiophene)s - new, very stable conducting polymers. *Adv. Mater.* **4**, 116 (1992).
12. Tang, C. W. & VanSlyke, S. A. Organic electroluminescent diodes. *Appl. Phys. Lett.* **51**, 913 (1987).
13. Tang, C. W., VanSlyke, S. A. & Chen, C. H. Electroluminescence of doped organic thin films. *J. Appl. Phys.* **65**, 3610 (1989).
14. Adamovich, V. I. et al. New charge-carrier blocking materials for high efficiency OLEDs. *Organic Electronics* **4**, 77 (2003).
15. Kulkarni, A. P., Tonzola, C. J., Babel, A. & Jenekhe, S. A. Electron Transport Materials for Organic Light-Emitting Diodes. *Chem. Mater.* **16**, 4556 (2004).

16. Kitamura, M. & Arakawa, Y. Pentacene-based organic field-effect transistors. *J. Phys. Condens. Matter* **20**, 184011 (2008).
17. Dimitrakopoulos, C. D., Purushothaman, S., Kymissis, J., Callegari, A. & Shaw, J. M. Low-Voltage Organic Transistors on Plastic Comprising High-Dielectric Constant Gate Insulators. *Science* **283**, 822 (1999).
18. Klauk, H. et al. High-mobility polymer gate dielectric pentacene thin film transistors. *J. Appl. Phys.* **92**, 5259 (2002).
19. Pope, M. & Swenberg, C. E. Electronic Processes In Organic-Solids. *Ann. Rev. Phys. Chem.* **35**, 613 (1984).
20. Schidleja, M., Melzer, C. & von Seggern, H. Electroluminescence from a pentacene based ambipolar organic field-effect transistor. *Appl. Phys. Lett.* **94**, 123307 (2009).
21. Muccini, M. A bright future for organic field-effect transistors. *Nat. Mater.* **5**, 605 (2006).
22. Repp, J., Meyer, G., Stojkovic, S. M., Gourdon, A. & Joachim, C. Molecules on Insulating Films: Scanning-Tunneling Microscopy Imaging of Individual Molecular Orbitals. *Phys. Rev. Lett.* **94**, 026803 (2005).
23. Soe, W.-H., Manzano, C., DeSarkar, A., Chandrasekhar, N. & Joachim, C. Direct observation of molecular orbitals of pentacene physisorbed on Au(111) by scanning tunneling microscope. *Phys. Rev. Lett.* **102**, 176102 (2009).
24. Gross, L., Mohn, F., Moll, N., Liljeroth, P. & Meyer, G. The chemical structure of a molecule resolved by atomic force microscopy. *Science* **325**, 1110 (2009).
25. Stipe, B. C., Rezaei, M. A. & Ho, W. Single-Molecule Vibrational Spectroscopy and Microscopy. *Science* **280**, 1732 (1998).
26. Gimzewski, J. K., Reihl, B., Coombs, J. H. & Schlittler, R. R. Photon emission with the scanning tunneling microscope. *Z. Physik B* **72**, 497 (1988).
27. Qiu, X. H., Nazin, G. V. & Ho, W. Vibrationally Resolved Fluorescence Excited with Submolecular Precision. *Science* **299**, 542 (2003).
28. Ćavar, E. et al. Fluorescence and Phosphorescence from Individual C_{60} Molecules Excited by Local Electron Tunneling. *Phys. Rev. Lett.* **95**, 196102 (2005).
29. Dong, Z. C. et al. Vibrationally Resolved Fluorescence from Organic Molecules near Metal Surfaces in a Scanning Tunneling Microscope. *Phys. Rev. Lett.* **92**, 086801 (2004).
30. Wu, S. W., Nazin, G. V. & Ho, W. Intramolecular photon emission from a single molecule in a scanning tunneling microscope. *Phys. Rev. B* **77**, 205430 (2008).

31. Ford, G. W. & Weber, W. H. Electromagnetic interactions of molecules with metal surfaces. *Phys. Rep. (Review Section of Physics Letters)* **113**, 195 (1984).
32. Rossel, F., Pivetta, M., Patthey, F. & Schneider, W.-D. Plasmon enhanced luminescence from fullerene molecules excited by local electron tunneling. *Opt. Express* **17**, 2714 (2009).
33. Chen, J. C. Introduction to Scanning Tunneling Microscopy (Oxford Science Publications, 2008).
34. Stroscio, J. A. & Kaiser, W. J. Scanning Tunneling Microscopy (Academic Press, Inc, 1993).
35. Lang, N. D. Apparent barrier height in scanning tunneling microscopy. *Phys. Rev. B* **37**, 10395 (1988).
36. Tersoff, J. & Hamann, D. R. Theory and Application for the Scanning Tunneling Microscope. *Phys. Rev. Lett.* **50**, 1998 (1983).
37. Binnig, G., Rohrer, H., Gerber, C. & Weibel, E. Surface Studies by Scanning Tunneling Microscopy. *Phys. Rev. Lett.* **49**, 57 (1982).
38. Zeng, C., Wang, H., Wang, B., Yang, J. & Hou, J. G. Negative differential-resistance device involving two C_{60} molecules. *Appl. Phys. Lett.* **77**, 3595 (2000).
39. Grobis, M., Wachowiak, A., Yamachika, R. & Crommie, M. F. Tuning negative differential resistance in a molecular film. *Appl. Phys. Lett.* **86**, 204102 (2005).
40. Lambe, J. & McCarthy, S. L. Light Emission from Inelastic Electron Tunneling. *Phys. Rev. Lett.* **37**, 923 (1976).
41. Berndt, R., Gimzewski, J. K. & Johansson, P. Inelastic tunneling excitation of tip-induced plasmon modes on noble-metal surfaces. *Phys. Rev. Lett.* **67**, 3796 (1991).
42. Berndt, R. & Gimzewski, J. K. The role of proximity plasmon modes on noble metal surfaces in scanning tunneling microscopy. *Surf.Sci.* **269-270**, 556 (1992).
43. Berndt, R. & Gimzewski, J. K. Electromagnetic Interactions of Metallic Objects in Nanometer Proximity. *Phys. Rev. Lett.* **71**, 3493 (1993).
44. Johansson, P., Monreal, R. & Apell, P. Theory for light emission from a scanning tunneling microscope. *Phys. Rev. B* **42**, 9210 (1990).
45. Berndt, R. et al. Atomic Resolution in Photon Emission Induced by a Scanning Tunneling Microscope. *Phys. Rev. Lett.* **74**, 102 (1995).
46. Nilius, N., Ernst, N. & Freund, H. J. Photon Emission Spectroscopy of Individual Oxide-Supported Silver Clusters in a Scanning Tunneling Microscope. *Phys. Rev. Lett.* **84**, 3994 (2000).

47. Nilius, N., Cörper, A., Bozdech, G., Ernst, N. & Freund, H. J. Experiments on individual alumina-supported adatoms and clusters. *Prog. Surf. Sci.* **67**, 99 (2001).
48. Schull, G., Becker, M. & Berndt, R. Imaging Confined Electrons with Plasmonic Light. *Phys. Rev. Lett.* **101**, 136801 (2008).
49. Chen, C., Bobisch, C. A. & Ho, W. Visualization of Fermi's Golden Rule Through Imaging of Light Emission from Atomic Silver Chains. *Science* **325**, 981 (2009).
50. Samuelson, L. et al. Scanning tunneling microscope and electron beam induced luminescence in quantum wires. *J.Vac.Sci.Technol. B* **12**, 2521 (1994).
51. Reinhardt, M., Schull, G., Ebert, P. & Berndt, R. Atomic resolution in tunneling induced light emission from GaAs(110). *Appl. Phys. Lett.* **96** 152107 (2010).
52. Berndt, R. et al. Photon emission from adsorbed C60 molecules with sub-nanometer lateral resolution. *Appl. Phys. A* **57**, 513 (1993).
53. Alvarado, S. F., Rieß, W., Seidler, P. F. & Strohriegl, P. STM-induced luminescence study of poly(p-phenylenevinylene) by conversion under ultraclean conditions. *Phys. Rev. B* **56**, 1269 (1997).
54. Dong, Z. C. et al. Generation of molecular hot electroluminescence by resonant nanocavity plasmons. *Nat. Phot.* **4**, 50 (2010).
55. Basché, T., Moerner, W. E., Orrit, M. & Talon, H. Photon antibunching in the fluorescence of a single dye molecule trapped in a solid. *Phys. Rev. Lett.* **69**, 1516 (1992).
56. Vogelgesang, M., PhD thesis, (Ecole Politechnique Fédérale de Lausanne, Lausanne, 2005).
57. Corso, M. et al. Boron Nitride Nanomesh. *Science* **303**, 217 (2004).
58. Ren, B., Picardi, G. & Pettinger, B. Preparation of gold tips suitable for tip-enhanced Raman spectroscopy and light emission by electrochemical etching. *Rev. Sci. Instrum.* **75**, 837 (2004).
59. Alvarado, S. F. & Renaud, P. Observation of spin-polarized-electron tunneling from a ferromagnet into GaAs. *Phys. Rev. Lett.* **68**, 1387 (1992).
60. Perronet, K., Schull, G., Raimond, P. & Charra, F. Single-molecule fluctuations in a tunnel junction: A study by scanning-tunneling microscopy-induced luminescence. *Europhys. Lett.* **74**, 313 (2006).
61. Hoffmann, G., Kroger, J. & Berndt, R. Color imaging with a low temperature scanning tunneling microscope. *Rev. Sci. Instrum.* **73**, 305 (2002).

62. Barbara, A., Lopez-Rios, T. & Quemerais, P. Near-field optical microscopy with a scanning tunneling microscope. *Rev. Sci. Instrum.* **76**, 023704 (2005).
63. Watkins, N. J., Long, J. P., Kafafi, Z. H. & Makinen, A. J. Fiber optic light collection system for scanning-tunneling-microscope-induced light emission. *Rev. Sci. Instrum.* **78**, 053707 (2007).
64. Steidtner, J. & Pettinger, B. High-resolution microscope for tip-enhanced optical processes in ultrahigh vacuum. *Rev. Sci. Instrum.* **78**, 103104 (2007).
65. Zhang, D. et al. Parabolic mirror-assisted tip-enhanced spectroscopic imaging for non-transparent materials. *J.Raman Spectrosc.* **40**, 1371 (2009).
66. Berndt, R. et al. Sub-nanometer lateral resolution in photon emission from C60 molecules on Au(110). *Surf.Sci.* **307**, 1033 (1994).
67. Kemerink, M. et al. Low temperature scanning-tunneling microscope for luminescence measurements in high magnetic fields. *Rev. Sci. Instrum.* **72**, 132 (2001).
68. Murashita, T. Novel conductive transparent tip for low-temperature tunneling-electron luminescence microscopy using tip collection. *J.Vac.Sci.Technol. B* **15**, 32 (1997).
69. Berndt, R., Schlittler, R. R. & Gimzewski, J. K. Photon emission scanning tunneling microscope. *J.Vac.Sci.Technol.* **9**, 573 (1991).
70. CoCreate. (CoCreate Software Inc. USA, 2006).
71. Kalkbrenner, T., Hakanson, U. & Sandoghdar, V. Tomographyic Plasmon Spectroscopy of a Single Gold Nanoparticel. *Nano Lett.* **4**, 2309 (2004).
72. Betzig, E. & Chichester, R. J. Single Molecules Observed by Near-Field Scanning Optical Microscopy. *Science* **262**, 1422 (1993).
73. Jasny, J. & Sepiol, J. Single molecules observed by immersion mirror objective. A novel method of finding the orientation of a radiating dipole. *Chem.Phys.Lett.* **273**, 439 (1997).
74. Pierce, D. T., Davies, A., Stroscio, J. A. & Celotta, R. J. Polarized light emission from the metal-metal STM junction. *Appl. Phys. A* **66**, 403 (1998).
75. Horcas, I. et al. WSxM: A software for scanning probe microscopy and a tool for nanotechnology. *Rev. Sci. Instrum.* **78**, 013705 (2007).
76. Berndt, R. & Gimzewski, J. K. Photon emission in scanning tunneling microscopy: Interpretation of photon maps of metallic systems. *Phys. Rev. B* **48**, 4746 (1993).
77. Branscheid, R., Jacobsen, V. & Kreiter, M. STM induced light from nontrivial metal structures:Local variations in emission efficiency. *Surf. Sci.* **602**, 176 (2008).

78. Hoffmann, G., Berndt, R. & Johansson, P. Two-Electron Photon Emission from Metallic Quantum Wells. *Phys. Rev. Lett.* **90**, 046803 (2003).
79. Berndt, R. & Gimzewski, J. K. Isochromat spectroscopy of photons emitted from metal surfaces in an STM. *Ann. Phys.* **505**, 133 (1993).
80. Shen, C., Kahn, A. & Schwartz, J. Chemical and electrical properties of interfaces between magnesium and aluminum and tris-(8-hydroxy quinoline) aluminum. *J. Appl. Phys.* **89**, 449 (2001).
81. Hill, I. G., Rajagopal, A., Kahn, A. & Hu, Y. Molecular level alignment at organic semiconductor-metal interfaces. *Appl. Phys. Lett.* **73**, 662 (1998).
82. Auwärter, W., Kreutz, T. J., Greber, T. & Osterwalder, J. XPD and STM investigation of hexagonal boron nitride on Ni(111). *Surf. Sci.* **429**, 229 (1999).
83. Schwennicke, C., Schimmelpfennig, J. & Pfnür, H. Morphology of thin NaCl films grown epitaxially on Ge(100). *Surf. Sci.* **293**, 57 (1993).
84. Slagle, O. D. & McKinstry, H. A. The lattice parameter in the solid solution KCl-KBr. *Acta Cryst.* **21**, 1013 (1966).
85. Repp, J., PhD thesis, (Freie Universität Berlin, Berlin, 2002).
86. Ohmann, R. et al. (in preparation).
87. Hebenstreit, W. et al. Atomic resolution by STM on ultra-thin films of alkali halides: experiment and local density calculations. *Surf. Sci.* 424, L321 (1999).
88. Dil, H. et al. Surface Trapping of Atoms and Molecules with Dipole Rings. *Science* **319**, 1824 (2008).
89. Wu, S. W., Nazin, G. V., Chen, X., Qiu, X. H. & Ho, W. Control of Relative Tunneling Rates in Single Molecule Bipolar Electron Transport. *Phys. Rev. Lett.* **93**, 236802 (2004).
90. Repp, J., Meyer, G., Paavilainen, S., Olsson, F. E. & Persson, M. Imaging Bond Formation Between a Gold Atom and Pentacene on an Insulating Surface. *Science* **312**, 1196 (2006).
91. Yamane, H. et al. Electronic structure at highly ordered organic/metal interfaces: Pentacene on Cu(110). *Phys. Rev. B* **76**, 165436 (2007).
92. Michaelson, H. B. The work function of the elements and its periodicity. *J. Appl. Phys.* **48**, 4729 (1977).
93. Bennewitz, R. et al. Aspects of dynamic force microscopy on NaCl/Cu(111): resolution, tip-sample interactions and cantilever oscillation characteristics. *Surf. Interface. Anal.* **27**, 462 (1999).

94. Pivetta, M., Patthey, F., Stengel, M., Baldereschi, A. & Schneider, W.-D. Local work function Moiré pattern on ultrathin ionic films: NaCl on Ag(100). *Phys. Rev. B* **72**, 115404 (2005).
95. Crocker, L., Wang, T. & Kebarle, P. Electron affinities of some polycyclic aromatic hydrocarbons, obtained from electron-transfer equilibria. *J. Amer. Chem. Soc.* **115**, 7818 (1993).
96. Schwoerer, M. & Wolf, H. C. Organic Molecular Solids (Wiley-VCH, 2007).
97. Dimitrakopoulos, C. D., Brown, A. R. & Pomp, A. Molecular beam deposited thin films of pentacene for organic field effect transistor applications. *J. Appl. Phys.* **80**, 2501 (1996).
98. Kakuta, H. et al. Electronic structures of the highest ocuupied molecular orbital bands of a pentacene ultrathin film. *Phys. Rev. Lett.* **98**, 247601 (2007).
99. Berkebile, S. et al. Electronic band structure of pentacene: An experimental and theoretical study. *Phys. Rev. B* **77**, 115312 (2008).
100. Mattheus, C. C. et al. Polymorphism in pentacene. *Acta Cryst.* ***C*57**, 939 (2001).
101. Tiago, M. L., Northrup, J. E. & Louie, S. G. Ab initio calculation of the electronic and optical properties of solid pentacene. *Phys. Rev. B* **67**, 115212 (2003).
102. Ruppel, L. et al. A defect-free thin film pentacene diode: Interplay between transport and scanning tunneling microscope tip tunneling injection. *J. Appl. Phys.* **102**, 033708 (2007).
103. He, R., Chi, X., Pinczuk, A., Lang, D. V. & Ramirez, A. P. Extrinsic optical recombination in pentacene single crystals: Evidence of gap states. *Appl. Phys. Lett.* **87**, 211117 (2005).
104. Heinecke, E., Hartmann, D. & Hese, A. Laser spectroscopy of free pentacene molecules. *J. Chem. Phys.* **118**, 113 (2003).
105. Lehnig, R. & Slenczka, A. Spectroscopic investigation of the solvation of organic molecules in superfluid helium droplets. *J. Chem. Phys.* **122**, 244317 (2005).
106. Wild, U. P., Guttler, F., Pirotta, M. & Renn, A. Single Molecule Spectroscopy - Stark-Effect of Pentacene in Para-Terphenyl. *Chem. Phys. Lett.* **193**, 451 (1992).
107. Geacintov, W. E., Burgos, J., Pope, I. M. & Strom, C. Heterofission of pentacene excited singlets in pentacene-doped tetracene crystals. *Chem. Phys. Lett.* **11**, 504 (1971).
108. Aoki-Matsumoto, T., Furuta, K., Yamada, T., Moriya, H. & Mizuno, K. Excitonic Photoluminescence in Pentacene Single Crystal. *Int. J. Mod. Phys. B* **15**, 3753 (2001).

109. He, R., Tassi, N. G., Blanchet, G. B. & Pinczuk, A. Fundamental optical recombination in pentacene clusters and ultrathin films. *Appl. Phys. Lett.* **87**, 103107 (2005).

110. Lang, D. V., Chi, X., Siegrist, T., Sergent, A. M. & Ramirez, A. P. Amorphouslike density of gap states in single-crystal pentacene. *Phys. Rev. Lett.* **93**, 086802 (2004).

111. Kuhnke, K., Becker, R., Epple, M. & Kern, K. C_{60} Exciton Quenching near Metal Surfaces. *Phys. Rev. Lett.* **79**, 3246 (1997).

112. Meyling, J. H., Hesselink, W. H. & Wiersma, D. A. Full anisotropy of the stark effect on the $^1B_{2u} \leftarrow ^1A_g$ electronic transitions of tetracene and pentacene in a ρ-terphenyl host crystal. *Chem. Phys.* **17**, 353 (1976).

113. Lindahl, J., Pistol, M. E., Montelius, L. & Samuelson, L. Stark effect in individual luminescent centers observed by tunneling luminescence. *Appl. Phys. Lett.* **68**, 60 (1996).

114. Hakanson, U., Hakanson, H., Johansson, M. K.-J., Samuelson, L. & Pistol, M. E. Electric field effects in single semiconductor quantum dots observed by scanning tunneling luminescence. *J. Vac. Sci. Technol. B* **21**, 2344 (2003).

115. Beham, E., Zrenner, A. & Böhm, G. STM-photocurrent-spectroscopy on single self-assembled InGaAs quantum dots. *Physica E* **7**, 359 (2000).

116. Limot, L., Maroutian, T., Johansson, P. & Berndt, R. Surface-State Stark shift in a STM. *Phys. Rev. Lett.* **91**, 196801 (2003).

117. Dougherty, D. B., Maksymovych, P., Lee, J. & Yates Jr., J. T. Stark-shifted image potential states of benzene bilayers on Cu(110) and Cu(111). *Chem. Phys. Lett.* **431**, 303 (2006).

118. Ogawa, S., Heike, S., Takahashi, H. & Hashizume, T. Tip-induced energy shift in Au/Fe(100) quantum wells. *Phys. Rev. B* **75**, 115319 (2007).

119. Prikhotko, A. F., Skorobogatko, A. F. & Tsikora, L. I. Spectra of Pentacene in Certain Crystalline Solvents. *Optics Spectrosc.* **26**, 115 (1969).

120. Tsiper, E. V. & Soos, Z. G. Electronic polarization in pentacene crystals and thin films. *Phys. Rev. B* **68**, 085301 (2003).

121. Sebastian, L., Weiser, G. & Bässler, H. Charge transfer transitions in solid tetracene and pentacene studied by electroabsorption. *Chem. Phys.* **61**, 125 (1981).

122. Varma, C. A. G. O. & Oosterhoff, L. J. The polarizability of tetracene in its first excited singlet state. *Chem-Phys.Lett.* **8**, 1 (1971).

123. Petelenz, B., Petelenz, P., Shurvell, H. F. & Smith Jr., V. H. Reconsideration of the electroabsorption spectra of the tetracene and pentacene crystals. *Chem.Phys.* **119**, 25 (1988).
124. Petelenz, P. Nonlocal polarizabilities in excited states of polyacene crystals. *Chem. Phys. Lett.* **215**, 607 (1993).
125. Gisslen, L. & Scholz, R. Crystallochromy of perylene pigments: Interference between Frenkel excitons and charge-transfer states. *Phys.Rev.B* **80**, 115309 (2009).
126. Schuster, R., Knupfer, M. & Berger, H. Exciton Band Structure of Pentacene Molecular Solids: Breakdown of the Frenkel Exciton Model. *Phys. Rev. Lett.* **98**, 037402 (2007).
127. Brown, R. H. & Twiss, R. Q. Correlation Between Photons In 2 Coherent Beams Of Light. *Nature* **177**, 27 (1956).
128. Fox, M. Quantum Optics, An Introduction (Oxford, 2006).
129. Kimble, H. J., Dagenais, M. & Mandel, L. Photon Antibunching in Resonance Fluorescence. *Phys. Rev. Lett.* **39**, 691 (1977).
130. Fleury, L., Segura, J.-M., Zumofen, G., Hecht, B. & Wild, P. U. Nonclassical Photon Statistics in Single-Molecule Fluorescence at Room Temperature. *Phys. Rev. Lett.* **84**, 1148 (2000).
131. Ambrose, W. P., Basche, T. & Moerner, W. E. Detection and spectroscopy of single pentacene molecules in a p-terphenyl crystal by means of fluorescence excitation. *J. Chem. Phys.* **95**, 7150 (1991).
132. Michler, P. et al. Quantum correlation among photons from a single quantum dot at room temperature. *Nature* **406**, 968 (2000).
133. Reischle, M. et al. Electrically pumped single-photon emission in the visible spectral range up to 80 K. *Opt. Express* **16**, 12771 (2008).
134. Kurtsiefer, C., Zarda, P., Mayer, S. & Weinfurter, H. The breakdown flash of silicon avalanche photodiodes-back door for eavesdropper attacks? *J. Mod. Opt.* **48**, 2039 (2001).
135. Link, S., Scholl, A., Jacquemin, R. & Eberhardt, W. Electron dynamics at a Ag/C_{60} metal-semiconductor interface. Solid State Communications **113**, 689 (2000).
136. Ishihara, S. et al. Relaxation dynamics of photoexcitations in C_{60} films. *Chem. Phys. Lett.* **295**, 475 (1998).
137. Wang, H. et al. Doped Organic Crystals with High Efficiency, Color-Tunable Emission toward Laser Application. *Crystal Growth & Design* **9**, 4945 (2009).

138. Murata, H. et al. Molecular Organic Light-Emitting Diodes Based on a Guest-Host Active Layer: Approaches for Enhancing Device Performance. *Mol. Cryst. Liq. Cryst. Sci. Technol., Sect. A* **353**, 567 (2000).

139. Hajime, N., Masatoshi, S., Hiroaki, N. & Chihaya, A. Emission Color Tuning in Ambipolar Organic Single-Crystal Field-Effect Transistors by Dye-Doping. *Adv. Funct. Mater.* **20**, 1610 (2010).

Abbreviations

STM	scanning tunneling microscopy
UHV	ultra high vacuum
LDOS	local density of states
OLED	organic light emitting diode
OFET	organic field-effect transistor
NIR	negative ion resonance
PIR	positive ion resonance
EA	electron affinity
IP	ionization potential
STE	self-trapped exciton
FE	Frenkel exciton
CT	charge-transfer
HBT	Hanburry-Brown and Twiss

Publications

Versatile Optical Access to the Tunnel Gap in a Low-Temperature STM
K.Kuhnke, A.Kabakchiev, W.Stiepany, F.Zinser, R.Vogelgesang, and K.Kern
(accepted, Rev. Sci. Instrum. 2010)

Electroluminescence from Individual Pentacene Nanocrystals
A. Kabakchiev, K. Kuhnke, T. Lutz, and K. Kern
(accepted, Chem. Phys. Chem. 2010)

Stark Shift in a Scanning Tunneling Microscope Reveals Exciton Mixing in an Organic Semiconductor
K. Kuhnke, A. Kabakchiev, T. Lutz, and K. Kern
(in preparation)

Acknowledgements

First, I would like to thank Prof. Klaus Kern, the director of my thesis, for giving me the opportunity to work on this project, for his ideas, and for his guidance and support during the time of the thesis.

I am grateful to Dr. Klaus Kuhnke, who supervised this work and introduced me to the world of experimental physics, UHV, STM, etc. With his expertise he contributed a lot to the successful development of the project. He took part in the measurements, the data evaluation and the analysis of the experiments. I am thankful for his ideas, permanent readiness for discussions and his great all-round support.

I also owe thanks to our group member Theresa Lutz for the nice atmosphere in the lab and fruitful collaboration in the project.

I would like to acknowledge valuable discussions with Prof. Jens Pflaum and for providing us with purified pentacene powder.

Thanks to Wolfgang Stiepany, Andreas Koch and Peter Andler for their support in solving various technical issues, Mr. Chaikevitch and Mr. Siemers for their help with the electrical components.

Thanks to Uta Schlickum for the valuable corrections on the text of the thesis.

I would like to thank Ivan Brihuega and Seth White for the nice time and atmosphere in our office as well as all the people from 6C11 for being around and being ready for discussions and help.

My special thanks go to my parents Valentina and Krasimir for their support in all respects during the years. I am grateful to my grandparents Elenka and Mincho, who were among my primary school teachers, and initiated my curiosity and motivation to learn natural sciences.

Finally, I would like to thank my family – Mariana and our son Alex, for being so patient during my long working days at the institute, and especially for the permanent moral support and inspiration they gave me.

Curriculum vitae

Name	Alexander Kabakchiev
Date of Birth	17.04.1978
Nationality	Bulgarian
2010	PhD thesis: *Scanning Tunneling Luminescence of Pentacene Nanocrystals*, EPF Lausanne, Switzerland
2006-2010	Research Assistant in the Prof. Dr. Klaus Kern's group at Max-Planck-Institute for Solid State Research, Stuttgart, Germany
2006	Diploma Thesis at the Max-Planck-Institute for Metal Research and Robert Bosch GmbH, Stuttgart, Germany
2000-2006	Diploma studies in materials science at the University of Stuttgart, Germany
1997-2000	Diploma studies in mechanical engineering at the Technical University of Sofia, Bulgaria
1992-1997	Konstantin Galabov German Language High School, Sofia, Bulgaria